

CEERS: MIRI deciphers the spatial distribution of dust-obscured star formation in galaxies at $0.1 < z < 2.5$

Benjamin Magnelli¹, Carlos Gómez-Guijarro¹, David Elbaz¹, Emanuele Daddi¹, Casey Papovich^{2,3}, Lu Shen^{2,3}, Pablo Arrabal Haro⁴, Micaela B. Bagley⁵, Eric F. Bell⁶, Véronique Buat⁷, Luca Costantin⁸, Mark Dickinson⁴, Steven L. Finkelstein⁵, Jonathan P. Gardner⁹, Eric F. Jiménez-Andrade¹⁰, Jeyhan S. Kartaltepe¹¹, Anton M. Koekemoer¹², Yipeng Lyu¹, Pablo G. Pérez-González⁸, Nor Pirzkal¹³, Sandro Tacchella^{14,15}, Alexander de la Vega¹⁶, Stijn Wuyts¹⁷, Guang Yang^{18,19}, L. Y. Aaron Yung^{9*}, and Jorge Zavala²⁰

(Affiliations can be found after the references)

Received ; accepted

ABSTRACT

Aims. We study the stellar (i.e., rest-optical) and dust-obscured star-forming (i.e., rest-mid-infrared) morphologies (i.e., sizes and Sérsic indices) of star-forming galaxies (SFGs) at $0.1 < z < 2.5$.

Methods. We combined *Hubble Space Telescope* (*HST*) images from the Cosmic Assembly Near-infrared Deep Extragalactic Legacy Survey (CANDELS) with *JWST* images from the Cosmic Evolution Early Release Science (CEERS) survey to measure the stellar and dust-obscured star formation distributions of 69 SFGs. Rest-mid-infrared (rest-MIR) morphologies were determined using a Markov chain Monte Carlo (MCMC) approach applied to the sharpest Mid-InfraRed Instrument (MIRI) images (i.e., shortest wavelength) dominated by dust emission ($S_{\nu}^{\text{dust}}/S_{\nu}^{\text{total}} > 75\%$), as inferred for each galaxy from our optical-to-far-infrared spectral energy distribution fits with CIGALE. Rest-MIR Sérsic indices were only measured for the brightest MIRI sources, that is, with a signal-to-noise (S/N) greater than 75 (35 galaxies). At a lower S/N , simulations do indeed show that simultaneous measurements of both the size and Sérsic index become less reliable. We extended our study to fainter sources (i.e., $S/N > 10$; 69 galaxies) by restricting our structural analysis to their rest-MIR sizes (Re_{MIR}) and by fixing their Sérsic index to a value of one.

Results. Our MIRI-selected sample corresponds to a mass-complete sample ($> 80\%$) of SFGs down to stellar masses $10^{9.5}$, $10^{9.5}$, and $10^{10} M_{\odot}$ at $z \sim 0.3$, 1, and 2, respectively. The rest-MIR Sérsic index of bright galaxies ($S/N > 75$) has a median value of $0.7_{-0.3}^{+0.8}$ (the range corresponds to the 16th and 84th percentiles), which is in good agreement with their median rest-optical Sérsic indices. The Sérsic indices as well as the distribution of the axis ratio of these galaxies suggest that they have a disk-like morphology in the rest-MIR. Galaxies above the main sequence (MS) of star formation (i.e., starbursts) have rest-MIR sizes that are, on average, a factor ~ 2 smaller than their rest-optical sizes (Re_{Opt}). The median rest-optical to rest-MIR size ratio of MS galaxies increases with their stellar mass, from $1.1_{-0.2}^{+0.4}$ at $\sim 10^{9.8} M_{\odot}$ to $1.6_{-0.3}^{+1.0}$ at $\sim 10^{11} M_{\odot}$. This mass-dependent trend resembles the one found in the literature between the rest-optical and rest-near-infrared sizes of SFGs, suggesting that it is primarily due to radial color gradients affecting rest-optical sizes and that the sizes of the stellar and star-forming components of SFGs are, on average, consistent at all masses. There is, however, a small population of SFGs ($\sim 15\%$) with a compact star-forming component embedded in a larger stellar structure, with $Re_{\text{Opt}}^c > 1.8 \times Re_{\text{MIR}}$. This population could be the missing link between galaxies with an extended stellar component and those with a compact stellar component, the so-called blue nuggets.

Key words. galaxies: evolution – galaxies: high-redshift – galaxies: structure – infrared: galaxies

1. Introduction

In the star formation rate (SFR)–stellar mass (M_*) plane, galaxies roughly divide into two groups, star-forming galaxies (SFGs) and quiescent galaxies (QGs). SFGs are mostly associated with disk-dominated systems (i.e., with Sérsic indices $n \sim 1$; e.g., Wuyts et al. 2011b) and they lie on a tight locus of the SFR– M_* plane, known as the main sequence (MS) of SFGs (e.g., Noeske et al. 2007; Elbaz et al. 2007; Schreiber et al. 2015; Barro et al. 2019, and references therein). The small scatter of the MS, observed out to $z \sim 4$ (Schreiber et al. 2015), suggests that secular evolution is the dominant mode of growth in SFGs, where gas inflow, outflow, and the star formation are in equilibrium (e.g., Bouché et al. 2010; Davé et al. 2012; Lilly et al. 2013; Peng & Maiolino 2014; Rathaus & Sternberg 2016). Conversely, QGs are mostly associated with massive bulge-dominated systems ($n \gtrsim 3$) with no or little star formation and they lie well below the MS (e.g., Wuyts et al. 2011b). The rest-optical sizes of

both SFGs and QGs show a tight but distinct scaling with galaxy stellar mass (e.g., van der Wel et al. 2014). At all masses, SFGs are larger than QGs, and their size–mass relation has a shallower slope and its intercept has a slower redshift evolution than those of QGs (e.g., van der Wel et al. 2014). Connecting progenitors and descendants implies that individual SFGs must have experienced a significant size growth (van Dokkum et al. 2013, 2015) while evolving along the MS, and that, on their way to quiescence, SFGs must experience a phase of significant compaction (e.g., Cheung et al. 2012; Barro et al. 2017; Mosleh et al. 2017). The mechanisms at the origin of this otherwise well-established structural evolution of SFGs are far from being clearly understood.

To investigate the processes leading to the structural evolution of SFGs, it is necessary to measure not only their current morphologies (i.e., those of their stellar components), but also the distribution of their ongoing star formation, as this allows us to predict their size growth (e.g., Wilman et al. 2020). To this end, tremendous efforts have been made over the past decade to

* NASA Postdoctoral Fellow

obtain unobscured star formation maps of large samples of high-redshift SFGs from their $H\alpha$ line emission using *Hubble Space Telescope* (*HST*) WFC3 grism spectroscopy or adaptive optics-assisted ground-based integral field unit surveys (e.g., Nelson et al. 2012, 2013; Tacchella et al. 2015; Nelson et al. 2016; Tacchella et al. 2018; Wilman et al. 2020; Matharu et al. 2022). All of these studies consistently find that the effective radius (R_e ; equivalently half-light radius) of the $H\alpha$ emission is slightly more extended than the stellar continuum, with a weak dependence on mass. In the absence of dust attenuation, such a profile would translate into a centrally depressed specific SFR (sSFR; i.e., SFR/M_*) and this would point to an inside-out growth of the stellar disk. However, SFGs at high redshifts are far from being devoid of dust and are therefore affected by nontrivial radial attenuation gradients (Wuyts et al. 2012; Nelson et al. 2016; Tacchella et al. 2018; Pérez-González et al. 2023; Zhang et al. 2023). By accounting for dust attenuation in these $H\alpha$ measurements, using either the Balmer decrement or the UV slope β , a converging picture is emerging, in which the sSFR profile of intermediate-mass ($\sim 10^{10-11} M_\odot$) galaxies is relatively flat—at odds with an inside-out growth scenario—and in which only massive ($\gtrsim 10^{11} M_\odot$) galaxies exhibit a centrally depressed sSFR, possibly associated with inside-out quenching (Tacchella et al. 2016, 2018).

Having in mind the effect of dust and the extreme difficulty of correcting for it using simple Balmer decrement or β -slope prescriptions for massive galaxies (i.e., $> 10^{10.5} M_\odot$; Wuyts et al. 2011a), other studies have focused their efforts in measuring the dust-obscured star formation distribution of SFGs from their dust emission using the Atacama Large Millimeter Array (ALMA; e.g., Simpson et al. 2015; Ikarashi et al. 2015; Hodge et al. 2016; Fujimoto et al. 2017; Gómez-Guijarro et al. 2018; Elbaz et al. 2018; Lang et al. 2019; Rujopakarn et al. 2019; Puglisi et al. 2019; Franco et al. 2020; Chang et al. 2020; Chen et al. 2020; Tadaki et al. 2020; Puglisi et al. 2021; Gómez-Guijarro et al. 2022a, see also Murphy et al. 2017; Jiménez-Andrade et al. 2019 for a radio view on this topic). Despite some quantitative differences, all of these studies qualitatively agree on the fact that high-redshift (i.e., $z \gtrsim 1$) massive ($M_* \gtrsim 10^{11} M_\odot$) SFGs have dust-obscured star formation distributed in regions which are significantly more compact relative to the size–mass relation of SFGs. Such compact star-forming core could correspond to the compaction phase that massive SFGs must experience prior to falling into quiescence. However, these results draw a very different picture from that which emerges from the $H\alpha$ observations, even after having accounted for dust attenuation. The reason for such inconsistencies could be twofold: (i) $H\alpha$ measurements could still be affected by non-recoverable dust attenuation effects in massive galaxies (e.g., Tacchella et al. 2022); and/or (ii) inconsistencies between the rest-(sub)millimeter and $H\alpha$ observations could be due to differences between samples that fit into a common evolutionary sequence. To make a significant step forward in this domain, we need to probe the dust-obscured star formation distribution of a larger number of SFGs at intermediate mass ($10^{10-11} M_\odot$). Unfortunately, such measurements have been difficult to obtain until now because the detection at high angular resolution of the dust emission from a large sample of SFGs at intermediate mass is observationally very expensive with the very small field of view of ALMA.

The Mid-InfraRed Instrument (MIRI) on board *JWST* (Gardner et al. 2006) with its unparalleled sensitivity and high angular resolution at mid-infrared (MIR) wavelengths offers a unique opportunity to make significant progress in this domain. The MIR emission probed by these observations is indeed dominated by

the polycyclic aromatic hydrocarbons (PAH) features of SFGs up to $z \sim 2.5$, which are known to provide relatively accurate measurements of the dust-obscured SFR (e.g., Elbaz et al. 2010, 2011; Nordon et al. 2012; Schreiber et al. 2018). Furthermore, the angular resolution of, for example, $0''.4$ at $15 \mu\text{m}$ (3.2 kpc at $z = 1$) should be sufficient to measure the Sérsic index (for the brightest galaxies) and effective radius of SFGs at $M_* \gtrsim 10^{9.5} M_\odot$, as these systems have effective radii larger than 3 kpc at rest-optical wavelength (e.g., van der Wel et al. 2014). The ability of MIRI to reveal the dust-obscured star formation morphology of high-redshift SFGs was unambiguously demonstrated by Shen et al. (2023, see also Liu et al. 2023). In their study, Shen et al. (2023) used preliminary MIRI observations from the Cosmic Evolution Early Release Science (CEERS) survey to successfully measure the dust-obscured star formation distribution of a UV-selected sample of 70 SFGs at $0.2 < z < 2.5$ and to compare these distributions to the unobscured star formation and stellar distributions. They find that the effective radii at rest-MIR are slightly smaller (10%) than those at rest-optical at high mass ($\sim 10^{10} M_\odot$) and find evidence that massive SFGs had an increased fraction of obscured star formation in their inner regions.

In this paper, we extend the analysis of Shen et al. (2023) to the full set of MIRI observations from CEERS (i.e., four pointings instead of two, covering a total of $\sim 8 \text{ arcmin}^2$) and focus on a mass-complete sample of SFGs instead of a UV-selected sample, which is biased against massive and strongly obscured SFGs. With this dataset, we measure the rest-MIR morphology of a mass-complete sample of 69 SFGs down to $\sim 10^{10} M_\odot$ and up to $z \sim 2.5$. At these intermediate masses, the fraction of unobscured star formation is subdominant ($\lesssim 30\%$; Whitaker et al. 2017; Shen et al. 2023, and our analysis) and, therefore, our rest-MIR morphologies trace, to first order, the total star-forming component of these SFGs. By comparing the size of the star-forming component of these SFGs to that of their stellar component, we obtain information about the growth of galaxies through cosmic time.

The structure of this paper is as follows. In Section 2, we present the MIRI and ancillary data used in this study and describe how we built our mass-complete sample of SFGs at $0.1 < z < 2.5$. In Section 3, we describe the method used to measure the structural parameters of our galaxies. In Sections 4.1 and 4.2, we present the main results of this study, that is, the rest-MIR Sérsic indices and sizes of SFGs and compare them to measurements at rest-optical wavelengths. In Section 5, we discuss the implications of our results for galaxy growth models. Finally, in Section 6, we present our summary.

Throughout this paper, we assume a concordance Λ CDM cosmology, adopting $H_0 = 70 \text{ (km/s)/Mpc}$, $\Omega_M = 0.30$ and $\Omega_\Lambda = 0.70$. At $z = 1$, $1''$ corresponds to 8.008 kpc . A Chabrier (2003) initial mass function (IMF) is used for all stellar masses and SFRs quoted in this article.

2. Data and sample

2.1. CEERS MIRI

In this work, we used the MIRI images produced by the CEERS team for their MIRI 1, 2, 5, and 8 fields (Finkelstein et al. 2023, the so-called red MIRI pointings), all in the Extended Groth Strip (EGS) field. The MIRI 1 and 2 fields benefit from observations with the F770W ($5\sigma \sim 25.6 \text{ AB}$), F1000W (~ 24.8), F1250W (~ 24.1), F1500W (~ 23.6), F1800W (~ 22.8),

and F2100W (~ 22.2) filters; while the MIRI 5 and 8 fields were observed with the F1000W (~ 24.6), F1250W (~ 23.6), F1500W (~ 23.0), and F1800W (~ 22.4) filters (Yang et al. 2023b). Each of these MIRI fields covered an area of approximately 2 arcmin² and the full width at half maximum are 0′′269 (F770W), 0′′328 (F1000W), 0′′420 (F1280W), 0′′488 (F1500W), 0′′591 (F1800W), and 0′′674 (F2100W) according to the *JWST* user documentation¹. The CEERS MIRI 3, 6, 7, and 9 fields (the so-called blue MIRI pointings) were not used in our analysis because they were taken only with the F560W and F770W filters and thus provide very limited coverage of the rest-MIR emission of high-redshift SFGs.

The data processing of the MIRI observations is presented in detail in Yang et al. (2023b). Here, we provide only the most relevant properties of this data analysis.

The MIRI observations were calibrated using the *JWST* calibration pipeline (Bushouse et al. 2022) version 1.7.2 and mostly the default parameters for stages 1 and 2. The background was estimated and then subtracted by taking advantage of the multiple images taken in the same bandpass but at different dither positions. The astrometric correction and stage 3 of the pipeline were then applied to produce the final mosaic, noise, and weight maps. Their grids are aligned to the *HST* Cosmic Assembly Near-infrared Deep Extragalactic Legacy Survey (CANDELS) v1.9 WFC3 and ACS images (Koekemoer et al. 2011) and use a pixel scale of 0′′09.

Source extraction was performed using the python package `photutils` in dual mode. The detection maps were obtained by creating so-called chi-squared detection images (Szalay et al. 1999), which are weighted combinations of all MIRI images available over each field, that is, F770W², F1000W, F1250W, F1500W, F1800W, and F2100W. The Kron aperture photometry in each passband was then obtained with `photutils` in dual mode using these chi-squared-based segmentation maps. Our final multiwavelength MIRI catalog contains 327 sources with a signal-to-noise (S/N) greater than 5 in at least one MIRI bandpass. Among these 327 sources, 47, 35, 73, 18, and 65 are detected in 2, 3, 4, 5, and 6 MIRI bandpasses (73% have ≥ 2 MIRI detections).

2.2. Ancillary data

Because the CEERS red MIRI pointings overlap only partially ($\sim 45\%$) with the CEERS NIRC*am* pointings, the optical-to-near-infrared (NIR) photometry of MIRI-detected galaxies was taken from the publicly available multiwavelength catalog of Stefanon et al. (2017) for the EGS. This catalog was built using the *HST* WFC3 and ACS data from CANDELS, the All-wavelength Extended Groth strip International Survey (AEGIS), and the 3D-*HST* programs. It is based on detections in the F160W band and reaches a depth of 26.62 AB in this band. Supplemented by observations from the Canada-France-Hawaii and Mayall Telescopes as well as from the *Spitzer Space Telescope*, it provides photometry in 23 broadbands from optical to NIR wavelengths. Based on this photometry, Stefanon et al. (2017) also provide robust photometric redshifts ($\Delta z/(1+z) \sim 0.02$) and stellar mass measurements for all sources in the catalog. Finally,

¹ <https://jwst-docs.stsci.edu/jwst-mid-infrared-instrument/miri-performance/miri-point-spread-functions>

² The F770W and F2100W images are not available for the MIRI 5 and 8 fields.

when available, Stefanon et al. (2017) also provide the spectroscopic redshifts of the sources.

We cross-matched our MIRI galaxy catalog with that of Stefanon et al. (2017), using search radii of 1′′. Among our 327 galaxies, 321 have an optical/NIR counterpart (16 of which have a spectroscopic redshift). The six galaxies without a counterpart are so-called *HST*-dark galaxies (Wang et al. 2019), which means that they are not detected in the *HST* F160W band (on which the catalog of Stefanon et al. is based) but clearly detected by *Spitzer*/IRAC. As *HST*-dark galaxies are mainly located at $z > 3$ (Gómez-Guijarro et al. 2022a) and therefore outside our redshift range of interest, we excluded them in the rest of our analysis.

We complemented the optical/NIR photometry with MIR-to-radio photometry from the so-called EGS super-deblended catalog of Le Bail et al. (in prep; see also Liu et al. 2018, Jin et al. 2018). This super-deblended technique is a prior-based multiwavelength fitting method that optimizes the number of priors fit in each band. This catalog provides photometry in the bandpasses of *Spitzer* (24 μ m from FIDEL; Magnelli et al. 2011), *Herschel* (100 and 160 μ m from PEP; Lutz et al. 2011; 250, 350, and 500 μ m from HerMES; Oliver et al. 2012), SCUBA2 (850 μ m from S2CLS; Geach et al. 2017; 450 and 850 μ m from Zavala et al. 2017), and AzTEC (1.1mm from Aretxaga et al. 2015). Because this catalog is based on optical-to-NIR priors from Stefanon et al. (2017), there exists a one-to-one correspondence between these two catalogs. Among our 321 MIRI detections with an optical/NIR counterpart, 94 have a $S/N > 3$ detection at 24 μ m and 32 have at least one $S/N > 3$ detection at far-infrared (FIR) or (sub)millimeter (submm) wavelengths. In absence of FIR or (sub)mm detections, we used 5σ upper limits for these bands in our spectral energy distribution (SED) fits (see Sect. 2.3).

Finally, the rest-optical morphology of our MIRI detections was obtained by cross-matching the position of these galaxies with the structural parameter (Sérsic index, size, ellipticity) catalog of van der Wel et al. (2014). This catalog, which was used for their analysis of the size–mass relation, is based on the CANDELS F125W and F160W imagings as processed by the 3D-*HST* team. These effective radii along the semi-major axis at a rest-frame wavelength of 5000 Å were calculated by correcting their observed F125W (for galaxies at $z < 1.5$) and F160W (for galaxies at $z > 1.5$) effective radii for negative color gradients (see equations 1 and 2 in van der Wel et al. 2014). We cross-matched these catalogs using a search radius of 1′′ and found counterparts for all our 321 galaxies. Above our mass-complete limits (see Sect. 2.4), the number of galaxies with rest-optical structural parameters flagged as “bad” in the catalog of van der Wel et al. (2014) is negligible (i.e., three out of 72 galaxies).

2.3. SED modeling with CIGALE

To construct our final sample (see Sect. 2.4) from these 321 MIRI detections with counterparts in the catalog of Stefanon et al. (2017), we first fit their photometry from optical to (sub)mm wavelengths using CIGALE (Boquien et al. 2019; Yang et al. 2020). In doing so, we fixed their redshifts to those inferred in Stefanon et al. and used a delayed star formation history with an optional exponential burst, the Bruzual & Charlot (2003) stellar model, the Calzetti (2001) attenuation law, the Draine et al. (2014) dust emission model (imposing energy balance) and the Stalevski et al. (2016) Active Galactic Nuclei (AGN type 1 and 2) SED model. As we included the AGN and dust emission mod-

Table 1. CIGALE input parameters

Module	Parameter	Symbol	Values
Star formation history sfhdelayed	Main stellar population e -folding time	τ_{main}	0.5, 1, 5 Gyr
	Main stellar population age	t_{main}	1, 3, 5, 7 Gyr
	Mass fraction of the late burst	f_{burst}	0, 0.1, 0.2, 0.3
Simple stellar population bc03	Initial mass function	–	Chabrier (2003)
	Metallicity	Z	0.02 (Solar)
Dust attenuation dustatt_calzleit	Color excess of stellar continuum	$E(B - V)$	0, 0.1, 0.3, 0.5, 0.7, 0.9, 1.1
Dust emission dl2014	PAH mass fraction	q_{PAH}	0.47, 1.12, 1.77, 2.50, 3.90
	Minimum radiation field	U_{min}	5, 12, 20, 30, 40
	Fraction of photodissociation region emission	γ	0.01, 0.05, 0.1, 0.5
AGN emission skirtor2016	Edge-on optical depth at 9.7 μm	$\tau_{9.7}$	3, 5, 7, 9, 11
	Viewing angle	θ_{AGN}	30°, 70°
	AGN contribution relative to the dust luminosity	f_{AGN}	0, 0.05, 0.15, 0.30, 0.45, 0.99

NOTE. — For parameters not listed here, default values have been adopted. We refer the reader to Boquien et al. (2019) for more details on the CIGALE input parameters.

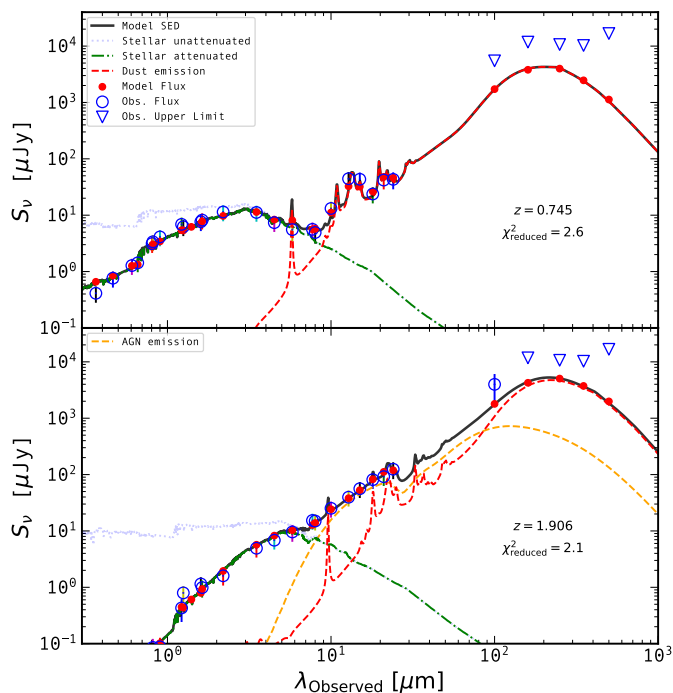


Fig. 1. Spectral energy distribution (SED) of two of our galaxies (*upper panel*: ID 12091; *lower panel*: ID 19062) as fit using CIGALE. Observed flux densities are shown by opened blue circles, while observed upper limits are shown by downward blue triangles. Black, red, orange, blue, and green lines correspond to the total, dust, AGN, stellar unattenuated and stellar attenuated emission, respectively. For the galaxy ID 12091, the AGN contribution (i.e., $L_{\text{AGN}}/(L_{\text{AGN}} + L_{\text{dust}})$) is of 0% and the sharpest MIRI band (shortest wavelength) dominated by dust emission (i.e., $S_{\nu}^{\text{dust}}/S_{\nu}^{\text{total}} > 75\%$) is the 10 μm band. For the galaxy ID 19062, the AGN contribution is of 30% and none of the MIRI bands is dominated by dust emission.

ules of CIGALE in our fits, this requires the generation of a very large number of models per galaxy. The parameter grids adopted

here (Tab. 1) have therefore been selected to obtain accurate fits, while keeping the number of models generated to a reasonable level. During the fit a minimum uncertainty of 10% is used to account for flux calibration uncertainties (Boquien et al. 2019). We inspected all 321 fits and found none significantly bad, consistent with the absence of outliers in their reduced χ^2 distribution. Figure 1 displays two examples of these fits, one for which the AGN contribution –i.e., $L_{\text{AGN}}/(L_{\text{AGN}} + L_{\text{dust}})$, where L_{AGN} and L_{dust} are the dust luminosity of the AGN and the dust luminosity of the host galaxy, respectively– is of 0% and one for which the AGN contribution is of 30%.

Based on these CIGALE best fits, we first excluded from our sample 60 galaxies with a significant contribution from an AGN (i.e., $L_{\text{AGN}}/(L_{\text{AGN}} + L_{\text{dust}}) \equiv f_{\text{AGN}} > 10\%$). The presence of these (obscured) AGNs was assessed by CIGALE thanks to their characteristic power-law rest-MIR emission (see lower panel of Fig. 1; see also, e.g., Donley et al. 2012; Yang et al. 2023a). The exclusion of these (obscured) AGNs prevents contamination in our morphological analysis, as their emission dominates in the rest-MIR, with $L_{\text{AGN}}[5 - 25\mu\text{m}]/(L_{\text{AGN}}[5 - 25\mu\text{m}] + L_{\text{dust}}[5 - 25\mu\text{m}]) \gtrsim 30\%$ (see the lower panel of Fig. 1). The fraction of (obscured) AGNs found in our study is consistent with the results of Yang et al. (2023a).

Using our CIGALE best fits, we then excluded from our sample 57 galaxies that are classified as quiescent based on their rest-optical colors and using a standard UVJ selection method (e.g., Mortlock et al. 2015). We note that one source was formally classified as quiescent using this UVJ selection but nevertheless detected in the MIR-to-FIR catalog of Le Bail et al. (in prep). This misclassified galaxy has been reintegrated in our sample of SFGs.

Finally, using our CIGALE best fits, we defined for each remaining galaxy which MIRI bands (if any) were dominated by dust emission, that is, $S_{\nu}^{\text{dust}}/S_{\nu}^{\text{total}} > 75\%$. For a given galaxy, when more than one MIRI band was dominated by dust emission, we adopted the band with the shortest wavelength (i.e., with the best angular resolution) for our rest-MIR structural measure-

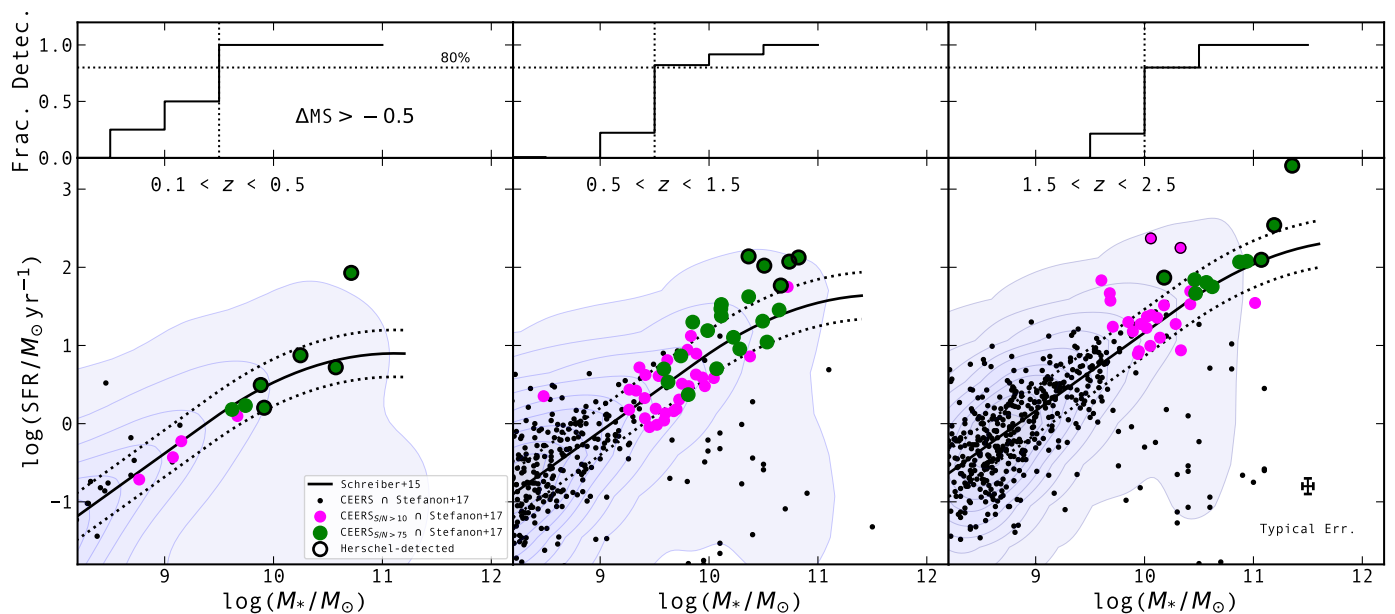


Fig. 2. Star formation rate vs. stellar mass distribution in three redshift ranges, i.e., $0.1 < z < 0.5$, $0.5 < z < 1.5$, and $1.5 < z < 2.5$ (lower panels). Filled green and magenta circles correspond to rest-MIR detection with $S/N > 75$ and $10 < S/N < 75$, respectively. Circles outlined by black edges are detected in the FIR by *Herschel* (i.e., with $S/N_{\text{FIR}} > 5$, where S/N_{FIR} is the signal-to-noise ratios added in quadrature from 100 to $500 \mu\text{m}$; Le Bail et al. in prep). Black dots show galaxies within the four CEERS red MIRI fields but which remained undetected in a MIRI bandpass that is dominated by dust emission (i.e., $S/N < 10$ or $S_{\nu}^{\text{dust}}/S_{\nu}^{\text{total}} < 75\%$). Shaded regions correspond to the distribution of all sources in the EGS, plotted using a kernel density estimator. The solid and dotted black lines show the MS of SFGs and its dispersion as inferred by Schreiber et al. (2015). (upper panels) Fraction of SFGs (i.e., $\Delta MS > -0.5$) as a function of stellar mass which are within the four CEERS red MIRI fields and are in our sample (i.e., that have at least one $S/N > 10$ MIRI detection dominated by dust emission). Our sample is 80% mass-complete down to $M_* \sim 10^{9.5}$, $10^{9.5}$, and $10^{10} M_{\odot}$ at $z \sim 0.3$, 1.0, and 2.0, respectively. A typical 1σ error bar for individual objects is shown in the right panel.

ments³. In the following, we refer to this band as the sharpest MIRI band (i.e., shortest wavelength) dominated by dust emission. For example, for the galaxy ID 12091 shown in the upper panel of Fig. 1, this corresponds to the MIRI $10 \mu\text{m}$ band (i.e., F1000W). Our sample contains 95 SFGs at $0.1 < z < 2.5$ that have a MIRI band dominated by dust emission and a detection significance in that band of $S/N > 10$ (i.e., the minimum detection significance required to accurately measure the rest-MIR size of a galaxy fixing its Sérsic index to 1; see Sect. 3); seven out of these 95 galaxies have a spectroscopic redshift. This number drops to 38 if we only consider bands with $S/N > 75$ (i.e., the minimum detection significance required to accurately measure both their rest-MIR sizes and Sérsic indices; see Sect. 3); two out of these 38 galaxies have a spectroscopic redshift.

In the rest of this analysis, the SFRs, stellar masses, and associated uncertainties of these 95 SFGs are taken from the CIGALE fits. We checked that these SFRs were consistent ($\sigma \sim 0.2$ dex) with those inferred by scaling the MS template of Elbaz et al. (2011) to the MIRI or *Herschel* flux densities of these galaxies. There are, however, three galaxies detected by *Herschel* for which CIGALE underestimated their SFR by a factor of three compared to those deduced from the FIR. For these galaxies, we used their *Herschel*-based SFRs instead.

2.4. Final sample

The SFR and stellar mass distributions of our sample of 95 SFGs that have a MIRI band dominated by dust emission and a detection significance in that band of $S/N > 10$ are shown in

Fig. 2. Our galaxies clearly follow the MS of SFGs but also include some starbursts located above this sequence. In the upper panels of Fig. 2, we studied the fraction of SFGs (i.e., $\Delta MS \equiv \log(SFR_{\text{gal}}(M_*, z)/SFR_{\text{MS}}(M_*, z)) > -0.5$) which are within the four CEERS red MIRI fields and are in our sample, that is, with at least one $S/N > 10$ MIRI detection dominated by dust emission. From this analysis, we find that even with our relatively strict rest-MIR detectability of $S/N > 10$, our sample is 80% mass-complete down to $M_* \sim 10^{9.5}$, $10^{9.5}$, and $10^{10} M_{\odot}$ at $z \sim 0.3$, 1.0, and 2.0, respectively. In fact, the ten SFGs (i.e., $\Delta MS > -0.5$) above these stellar masses that do not appear in our sample are AGNs that we excluded because a detailed analysis of their host galaxy's rest-MIR morphology was practically impossible, $L_{\text{AGN}}[5-25 \mu\text{m}]/(L_{\text{AGN}}[5-25 \mu\text{m}] + L_{\text{dust}}[5-25 \mu\text{m}]) \geq 30\%$. Our sample should therefore be representative of the population of SFGs at intermediate mass ($\sim 10^{10-11} M_{\odot}$). At higher stellar masses, although our sample is complete, it still suffers from cosmic variance and misses the rare massive SFGs ($\geq 10^{11} M_{\odot}$) due to the small areal coverage of our MIRI observations.

For ease of interpretation, in the remainder of the analysis we restricted our sample to galaxies above these mass-complete limits of $M_* \sim 10^{9.5}$, $10^{9.5}$, and $10^{10} M_{\odot}$ at $z \sim 0.3$, 1.0, and 2.0, respectively. This sample, which originally contains 72 galaxies with robust rest-MIR structural measurements, drops to 69 galaxies when we consider only galaxies with rest-optical structural measurements not flagged as bad in the catalog of van der Wel et al. (2014). This mass-complete sample of 69 SFGs with robust rest-optical and rest-MIR structural measurements is our final sample. This final sample is, when needed, further segregated according to the MIRI detection significance (69 with $S/N > 10$ and 35 with $S/N > 75$).

³ Adopting instead the band with the longest wavelength would not change the results presented in this paper.

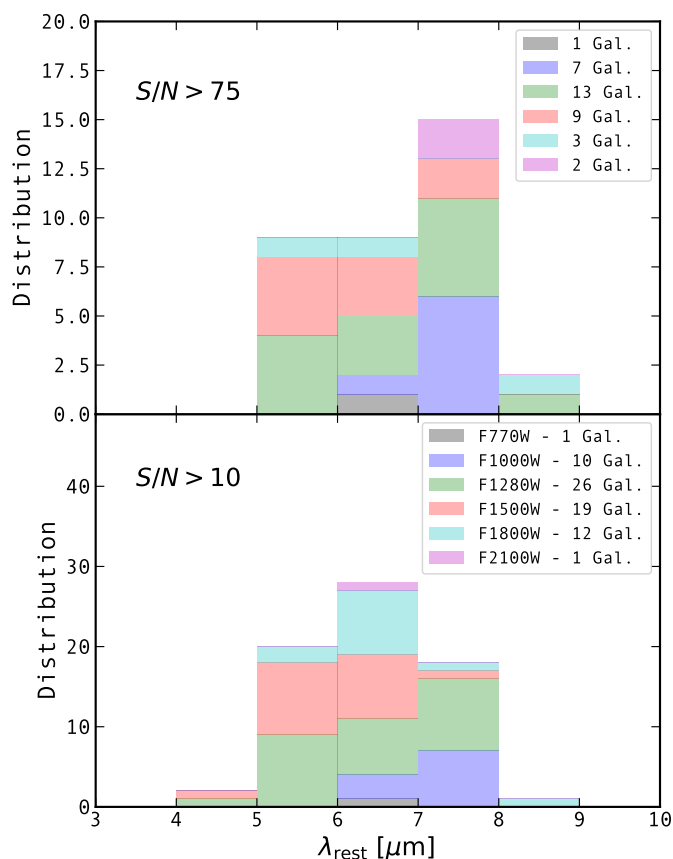


Fig. 3. Distributions of rest-MIR wavelengths probed by the sharpest MIRI band (shortest wavelength) with a detection dominated by dust emission, for our $S/N > 75$ (upper panel) and $S/N > 10$ (lower panel) samples. The colors of these stacked distributions correspond to the MIRI band used. The total number of galaxies in a given MIRI band is shown in the legend of each panel.

Figure 3 shows the distribution of rest-MIR wavelengths used for the morphological analysis of this final sample, that is, the wavelengths probed by their sharpest MIRI band dominated by dust emission. These rest-MIR wavelengths correspond mainly to the PAH 6.2 and 7.7 μm features, which implies that for galaxies located at a higher redshift, we use MIRI bands at longer (redder) effective wavelengths. This does not seem to affect our results, as none of the trends observed in the paper depend on the redshift of our galaxies.

Finally, using the CIGALE best fits of these 69 SFGs, we studied the fraction of their SFR that is obscured by dust, $\text{SFR}_{\text{IR}}/(\text{SFR}_{\text{UV}} + \text{SFR}_{\text{IR}})$, where SFR_{IR} is the dust-obscured SFR and is given by $\text{SFR}_{\text{IR}}[M_{\odot} \text{yr}^{-1}] = 1.09 \times 10^{-10} \times L_{\text{dust}}[8 - 1000 \mu\text{m}; L_{\odot}]$, while SFR_{UV} is the unobscured SFR and is obtained from the rest-frame luminosity at 2300 \AA , L_{UV} , as $\text{SFR}_{\text{UV}}[M_{\odot} \text{yr}^{-1}] = 3.6 \times 10^{-10} \times L_{\text{UV}}[L_{\odot}]$ (Kennicutt 1998). We found a median value of $0.89^{+0.06}_{-0.20}$ for $\text{SFR}_{\text{IR}}/(\text{SFR}_{\text{UV}} + \text{SFR}_{\text{IR}})$ (the range correspond to the 16th and 84th percentiles). This is consistent with literature results for the same stellar mass range as that probed by our final sample (see, e.g., Whitaker et al. 2017; Shen et al. 2023). In what follows, we therefore consider the star-forming component of our galaxies to be accurately traced by their dust-obscured star-forming component.

3. Structural parameter measurements

To constrain the rest-MIR structural parameters of our galaxies, we performed a standard Bayesian analysis using the python Markov chain Monte Carlo (MCMC) package *emcee* (Foreman-Mackey et al. 2013). For each galaxy, we started from the analytical formula of a Sérsic profile (defined by its Sérsic index, effective radius, ellipticity, and position), convolved the model to be tested with the point spread function (PSF) of the corresponding MIRI band, and finally calculated the likelihood of this model (i.e., $\exp(-\chi^2/2)$) by comparison with the real image assuming that the noise in the MIRI image is Gaussian. These noise maps are based on the weight maps generated by the *JWST* pipeline but we multiplied them by a factor $\sim 2 - 3$ (depending on the field and band) to account for pixel-correlated noise (Yang et al. 2023b). Given that the number density of stars in our MIRI images (especially in the longest bandpass) is relatively low and that we only have four MIRI fields covering a total of $\sim 8 \text{ arcmin}^2$, creating an empirical PSF is impractical. As an alternative, we used PSFs generated using *WebbPSF* (Perrin et al. 2014), assuming a pixel scale of $0''.09$ and accounting for the position angle of the different CEERS exposures. To perform our fits, we used cutouts of $5'' \times 5''$ centered on each of our galaxies. Our complete Sérsic model has seven parameters: the x and y offset from the center of the cutout, the total flux (S_{ν}), the Sérsic index (n), the effective radius (Re), the ellipticity (i.e., $\varepsilon = 1 - b/a$), and the position angle (PA). We adopted the effective radius along the semi-major axis to avoid inclination and projection effects. To account for the impact of neighboring sources, we performed our analysis three times. In the first pass, we fit all sources with $S/N > 10$ without considering neighboring sources and fixing the Sérsic index of sources with $10 < S/N < 75$ (see below) to 1. In the second and third passes, we fit each cutout after subtracting neighboring sources using their structural parameters found in the previous pass. The models converge after three passes.

An example of this structural analysis for one of our bright ($S/N > 75$) galaxies is shown in Fig. 4. It illustrates the advantage of this MCMC approach from which we can recover the complete posterior probability distribution and analyze covariance between parameters. In what follows, we use the 50th percentile as the best fit and the 16th and 84th percentiles as errors. We visually inspected all models (i.e., cutouts and residual cutouts) and found no problematic fit.

We validated our structural parameter measurements using Monte Carlo simulations. These simulations are based on the observed flux densities of our galaxies in the sharpest MIRI bandpass dominated by dust emission and their rest-optical structural parameters as taken from the structural parameter catalogs of van der Wel et al. (2014, ; see Sect. 2.2). For each galaxy, we proceeded as follows: from its MIRI flux density and rest-optical structural parameters, we created its mock light profile and introduced it in 100 different positions of the MIRI image, avoiding real sources using the corresponding segmentation map; then we retrieved the structural parameters of these 100 light profiles and compared the intrinsic and measured structural parameters.

With this set of simulations, we first assessed the lowest S/N below which accurate Sérsic index measurements could be obtained. We find that at $S/N < 75$ the quality of our measurements significantly degraded, driven especially by inaccurate Sérsic index measurements (relative error $> 50\%$). In what follows, we thus restricted our full structural analysis (i.e., n , Re , and ε) to our brightest 35 sources with $S/N > 75$. We note that such restriction is fully consistent with the analysis of van der Wel et al.

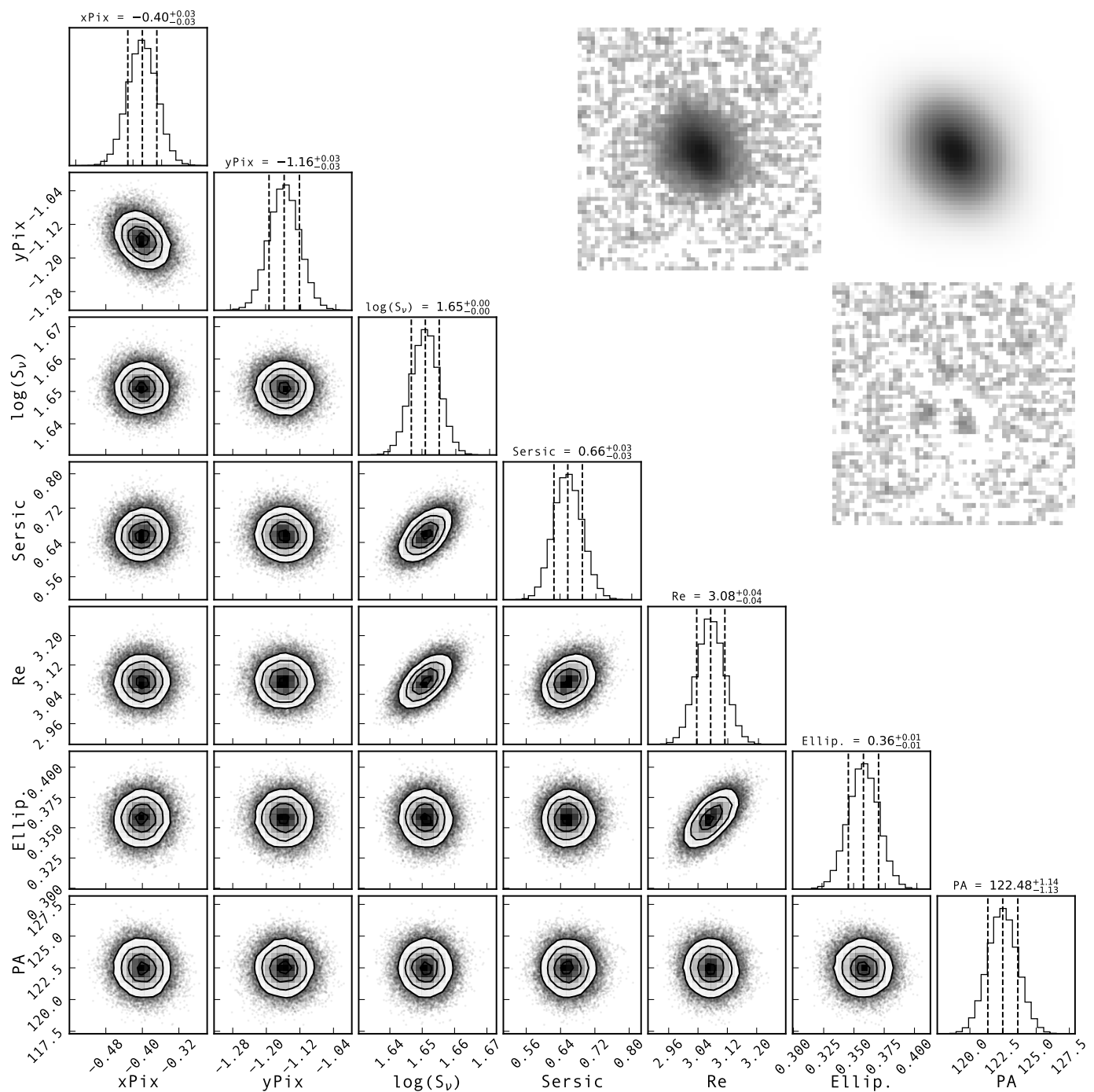


Fig. 4. Probability distributions of the structural parameters of one of our galaxies (ID 12091). From left to right, x and y -offset from the center of the $5'' \times 5''$ cutout ([pixel] with a pixel scale of $0''.09$), total flux ($[\log(\mu Jy)]$), Sérsic index, effective radius ([kpc]), ellipticity, and position angle ([degree]). This galaxy is bright enough (i.e., $S/N > 75$) that we let its Sérsic index as a free parameter. The dashed vertical lines show the 16th, 50th, and 84th percentiles of each distribution. The upper right panels show the original, model, and residual (original minus model) images of this galaxy in the $10 \mu\text{m}$ band.

(2014), who also restricted their Sérsic index measurements to sources 2 to 3 magnitude brighter than their 5σ detection threshold (i.e., $S/N > 30 - 75$).

In the first two rows of Fig. 5, we present the results of this first set of simulations, restricted to galaxies with $S/N > 75$. Our method accurately retrieves all three structural parameters across the entire dynamic range tested by our simulations, with a median in-to-out parameter ratio of $1.00^{+0.07}_{-0.16}$, $1.00^{+0.03}_{-0.03}$, and $1.00^{+0.07}_{-0.05}$ (the ranges correspond to the 16th and 84th percentiles)

for n , Re , and ε , respectively. Furthermore, not only our method accurately retrieves these structural parameters but it also provides accurate error measurements as specifically demonstrated by the second row of Fig. 5. Indeed, the true (i.e., $\Delta\text{Param} = \text{Param}_{\text{in}} - \text{Param}_{\text{out}}$) to estimated (i.e., σ_{Param}) error ratio follows a Gaussian distribution centered at zero and with a dispersion of one, as expected in the case of accurate error measurements.

To extend our morphological analysis to galaxies with $S/N < 75$, we limited our structural parameter measurements to their

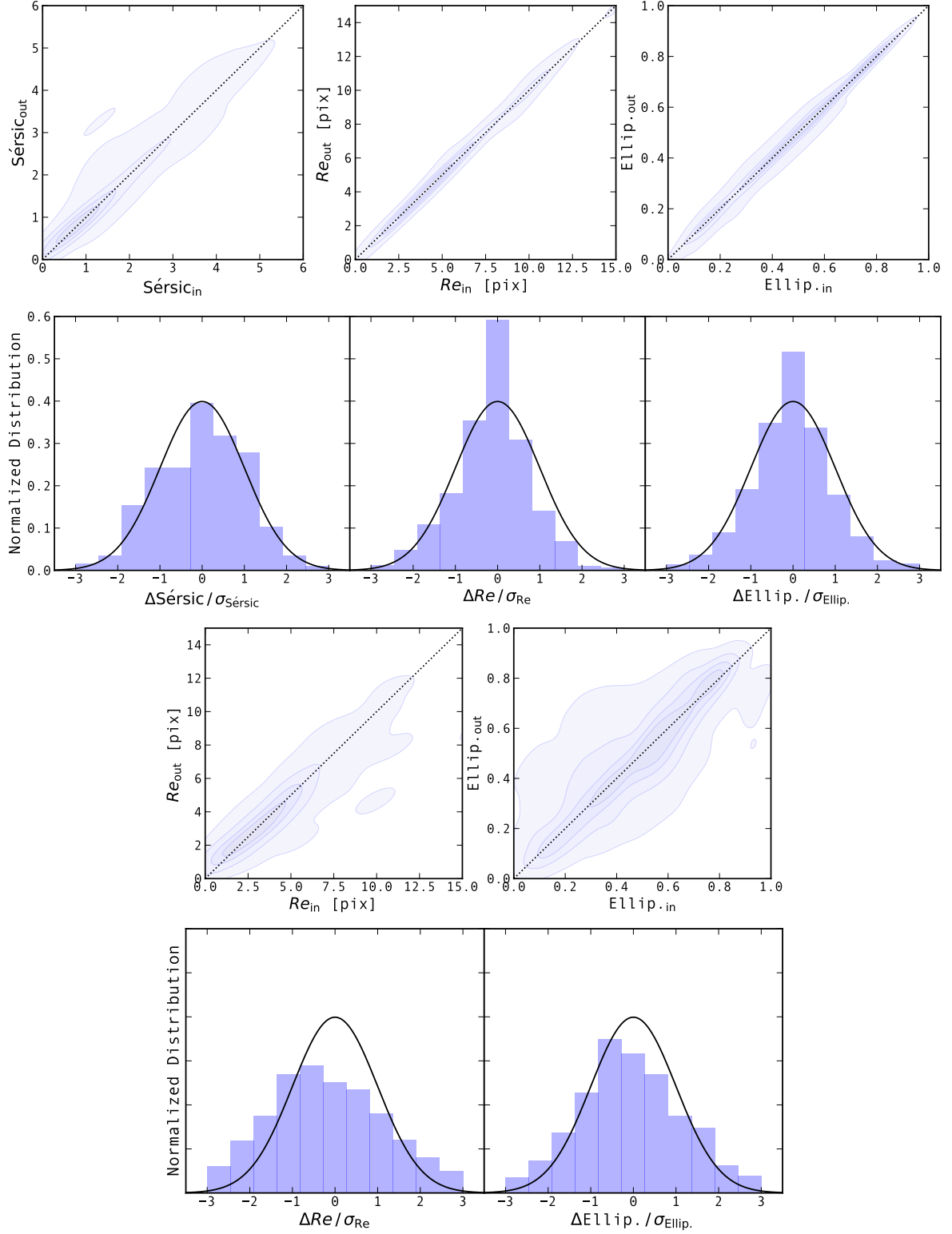


Fig. 5. Quality of our structural parameter measurements as inferred using Monte-Carlo simulations. (*1st row*) Comparison between the intrinsic (“in”) and measured (“out”) Sérsic indices, effective radii, and ellipticities. Shaded regions correspond to the distribution of all 3,500 simulated data points, plotted using a kernel density estimator. Dotted lines show the one-to-one relation. (*2nd row*) Distribution of the true (i.e., $\Delta\text{Param} = \text{Param}_{\text{in}} - \text{Param}_{\text{out}}$) to estimated (i.e., σ_{Param}) error ratio (blue histogram). The solid line shows a Gaussian distribution centered on zero and with a dispersion of one, i.e., the distribution that should be followed by the blue histogram if the estimated errors were statistically accurate. In the first two rows, mock galaxies were simulated using the observed rest-MIR flux density of each galaxy with $S/N > 75$ in our sample and their respective rest-optical Sérsic indices and sizes. Structural parameters were then retrieved using the MCMC approach described in Sect. 3. (*3rd row* and *4th row*) Same as the first two rows but for simulations performed using the observed rest-MIR flux density of galaxies with $10 < S/N < 75$ and their respective rest-optical Sérsic indices and sizes. Structural parameters were then retrieved using the MCMC approach described in Sect. 3 but fixing the Sérsic index to 1.

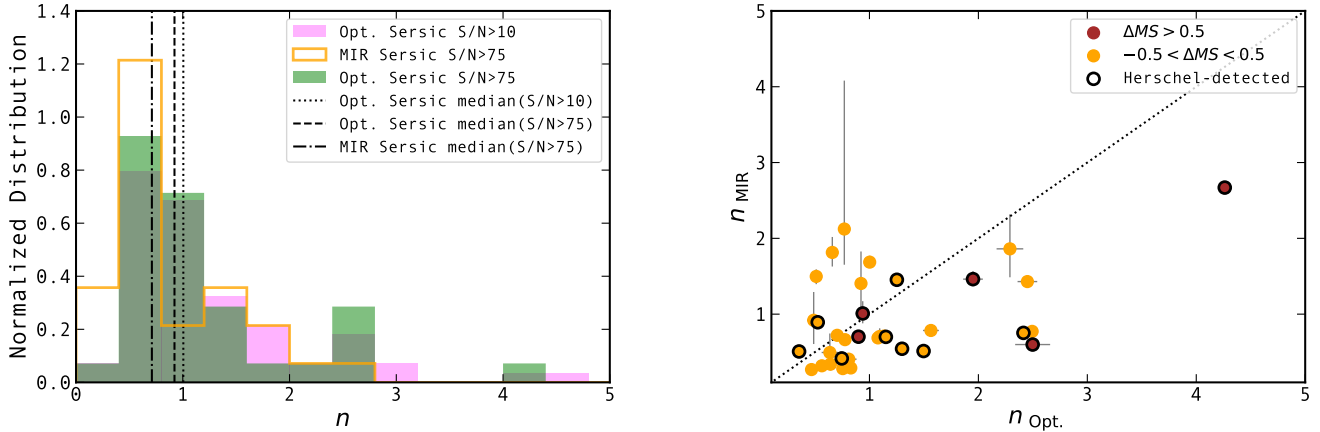


Fig. 6. Sérsic indices of our final sample. (*left*) Distributions of the rest-optical and rest-MIR Sérsic indices for our final sample. The green and magenta distributions correspond to the rest-optical Sérsic indices of our $S/N > 75$ and $S/N > 10$ samples, respectively. The orange distribution corresponds to the rest-MIR Sérsic indices of our $S/N > 75$ sample. The vertical dashed, dotted and dash-dotted lines show the median Sérsic indices of these distributions. (*right*) Comparison of the rest-MIR and rest-optical Sérsic indices of the 35 SFGs with $S/N > 75$ in our final sample. Circles are color-coded by the distance of each galaxy to the MS, i.e., $-0.5 < \Delta MS < 0.5$ (orange), and $\Delta MS > 0.5$ (brown). Circles outlined by black edges are detected in the FIR by *Herschel*.

effective radii and ellipticities by fixing the value of their Sérsic index. We decided to fix n_{MIR} to a value of 1 (exponential light profile⁴) because SFGs are known to be dominated by exponential light profiles, as demonstrated by the rest-optical and rest-MIR Sérsic index distributions of our sample (Fig. 6; Sect 4.1).

Using the same set of simulations, we then evaluated the quality of our radius and ellipticity measurements when fixing n_{MIR} to 1. First, we found that at $S/N < 10$ the quality of our R_e measurements significantly degraded and so restricted our partial structural parameter analysis (i.e., R_e and ε with $n_{\text{MIR}} = 1$) to sources with $S/N > 10$. The quality of our partial structural parameter analysis for galaxies with $S/N > 10$ is shown in the bottom two rows of Fig. 5. Our radius and ellipticity measurements are accurate with a median in-to-out parameter ratio of $0.99^{+0.22}_{-0.18}$ and $0.99^{+0.28}_{-0.27}$, respectively. However, these measurements are characterized by larger dispersions due in part to the lower S/N but also to our $n_{\text{MIR}} = 1$ assumption, which necessarily propagates into measurement inaccuracies ($n_{\text{in}} \neq 1$). Our errors are also affected by this assumption, with the distributions of the true to estimated errors ratio following Gaussian distributions centered on 0 but with dispersions of ~ 1.1 . We conclude that our errors are underestimated by $\sim 10\%$ (see also Sect. 4.1) because they do not account for the systematic error introduced by our $n_{\text{MIR}} = 1$ assumption. However, this effect remains relatively moderate because the galaxies in our sample have a median rest-optical Sérsic index close to a value of one. In what follows, we decided to simply increase by 10% the errors associated with our partial structural parameter analysis.

4. Results

4.1. Rest-MIR Sérsic indices

From the full structural parameter analysis performed on our $S/N > 75$ sample, we can study for the first time the rest-MIR Sérsic indices of 35 mass-complete SFGs at $0.1 < z < 2.5$.

⁴ Fixing instead the Sérsic index of each of our galaxies to that observed in the rest-optical would not change any of the results presented in this paper.

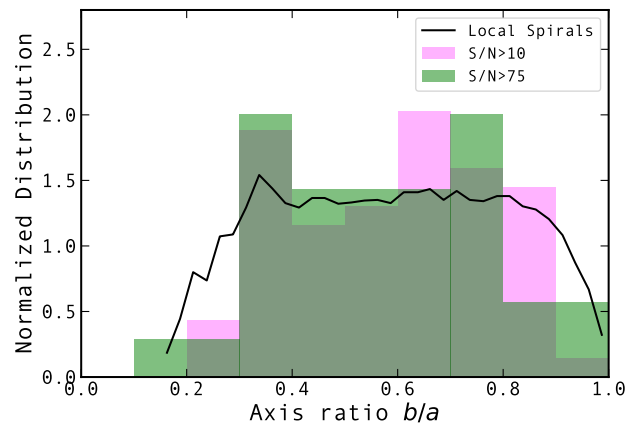


Fig. 7. Rest-MIR axis ratio (i.e., $b/a = 1 - \varepsilon$) distributions of our final sample. The green and magenta distributions correspond to our $S/N > 75$ and $S/N > 10$ samples, respectively. The black solid line shows the rest-optical axis ratio distribution of local spirals (Rodríguez & Padilla 2013).

The distribution of these rest-MIR Sérsic indices is shown in the left panel of Fig. 6 and is compared to that observed in the rest-optical.

The rest-MIR light profiles of our SFGs are mostly consistent with exponential light profiles, with a median n_{MIR} value of $0.7^{+0.8}_{-0.3}$ (here and hereafter, the range corresponds to the 16th and 84th percentiles). None of our galaxies have a rest-MIR Sérsic index compatible with a bulge-like light profile (i.e., $n \gtrsim 3$), although our simulations has shown that if they exist, we should be able to measure them (Sect. 3). The rest-MIR axis ratio distribution (i.e., $b/a = 1 - \varepsilon$; Fig. 7) of our SFGs follows that of local spirals (e.g., Rodríguez & Padilla 2013). Together with their exponential light profiles, this demonstrates that these SFGs have a disk-like morphology in the rest-MIR. We cannot, however, rule out the presence of a sub-dominant bulge-like star-forming core in these galaxies, because with the angular resolution and

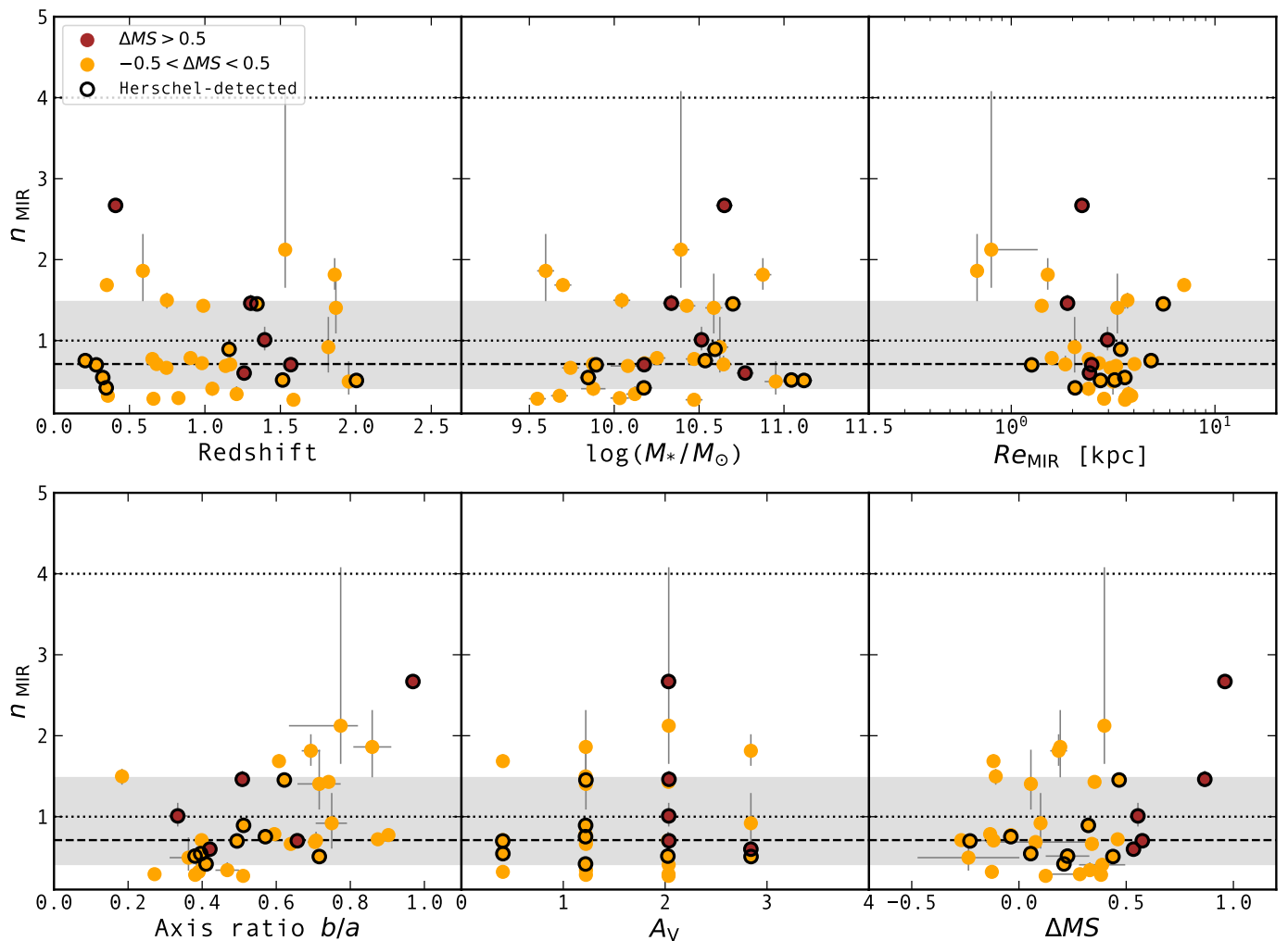


Fig. 8. Rest-MIR Sérsic indices of the 35 SFGs with $S/N > 75$ in our final sample as a function of their redshifts, stellar masses, rest-MIR effective radii, axis ratio, dust attenuation, and distances to the MS. Circles are color-coded by the distance of each galaxy to the MS, i.e., $-0.5 < \Delta MS < 0.5$ (orange), and $\Delta MS > 0.5$ (brown). Circles outlined by black edges are detected in the FIR by *Herschel*. The shaded regions show the 16th to 84th percentiles of the rest-MIR Sérsic index distribution, while the horizontal dashed lines represent its 50th percentile. The horizontal dotted lines correspond to the canonical disk-like ($n = 1$) and bulge-like ($n = 4$) Sérsic values. The discretized values along the dust attenuation axis correspond to the sampling of this parameter used for our CIGALE fits (see Sect. 2.3).

S/N of these MIRI observations, we are unable to perform robust double-component Sérsic fits.

The rest-MIR Sérsic index distribution resembles that observed in the rest-optical, although the latter is shifted toward slightly higher values with a median $n_{\text{Opt.}}$ of $0.9^{+1.2}_{-0.3}$. However, a two-sample Kolmogorov-Smirnov (KS) analysis cannot rule out that these two samples are drawn from the same distribution (p -value = 0.20). While these rest-MIR and rest-optical Sérsic index distributions agree as a population, this agreement is reduced when considering each galaxy individually (right panel of Fig. 6). Indeed, the relation between n_{MIR} and $n_{\text{Opt.}}$ is characterized by a mild correlation and a relatively large dispersion. This suggests that while both the stellar and dust-obscured star-forming components of these galaxies have a disk-like morphology, their exact spatial distributions are intrinsically different.

We then studied the possible correlation between the rest-MIR Sérsic indices of galaxies and some of their key physical properties such as their redshift, stellar mass, rest-MIR size, axis ratio, dust attenuation (A_V), and distance to the MS (Fig. 8). We find no clear correlation, although the small number statistics

offered by our $S/N > 75$ sample may hide subtle relations to some extent.

Finally, we tested on this sample the impact of fixing n_{MIR} to a value of one during our partial structural parameter analysis. In Fig. 9, we compare the effective radius inferred for these 35 galaxies using our full and partial structural parameter analysis. Fixing n_{MIR} to a value of one does not seem to introduce any significant and systematic bias into our partial structural parameter analysis. The inferred radii ratio has a mean value of 0.98 and a dispersion of 0.10. As already mentioned, this moderate impact is due to the fact that our SFGs intrinsically have Sérsic indices very consistent with a value of one and that $\Delta Re/\Delta n$ remains low when $n \sim 1$ and $\Delta n < 1$. Nevertheless, this systematic error is not accounted for in our statistical error measurements. We thus scaled these statistical errors by a factor of 1.1 in our partial structural parameter analysis.

4.2. Rest-MIR sizes

By running our partial structural parameter analysis on all $S/N > 10$ galaxies, we now extend our study to our mass-complete sam-

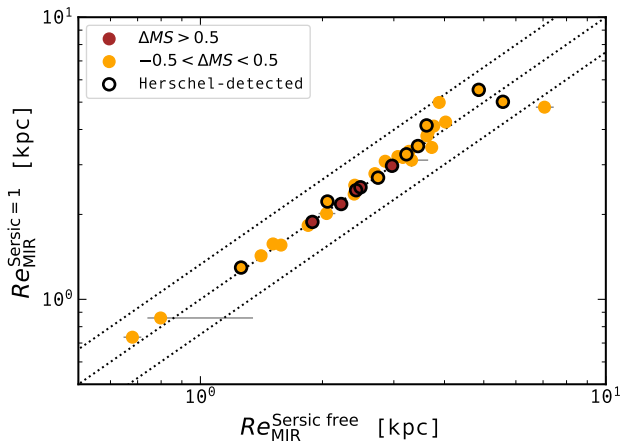


Fig. 9. Comparison between the effective radius inferred by setting or not n_{MIR} to a value of 1 when fitting the 35 SFGs with $S/N > 75$ in our final sample. Circles are color-coded by the distance of each galaxy to the MS, i.e., $-0.5 < \Delta MS < 0.5$ (orange), and $\Delta MS > 0.5$ (brown). Circles outlined by black edges are detected in the FIR by *Herschel*. The dotted lines show the one-to-one relation and relative errors of $\pm 33\%$.

ple of 69 SFGs at $0.1 < z < 2.5$. Although the Sérsic indices of these galaxies are fixed to a value of one, we can recover their effective radii and ellipticities, as we have shown in Sect. 3 and 4.1.

4.2.1. Size–mass relations

One of the most fundamental relations involving the effective radius of galaxies is the so-called size–mass relation (e.g., van der Wel et al. 2014). In the upper panels of Fig. 10, we present the rest-MIR size vs. mass distribution in our sample and compare it to the rest-optical size–mass relation inferred by van der Wel et al. (2014). To first order, our rest-MIR size vs. mass distribution is characterized by an increase of the rest-MIR sizes with stellar mass. However, at high stellar masses, our galaxies appear to have smaller rest-MIR sizes than those predicted by the rest-optical size–mass relation, and some of our galaxies even have rest-MIR sizes that are as small as those predicted for quiescent galaxies. Because this finding could, nevertheless, be due to a combination of small number statistics and a relatively large dispersion in the rest-optical size–mass relation, we also show in the lower panels of Fig. 10, the rest-optical size vs. mass distribution in our sample. In doing so, we unambiguously reveal that while for low stellar masses ($\lesssim 10^{10.5} M_{\odot}$), the rest-MIR and rest-optical sizes are consistent within the uncertainties, for high stellar masses, the rest-MIR sizes are significantly smaller than those at rest-optical wavelengths (see open squares and diamonds). This finding is qualitatively and quantitatively in line with the results of Shen et al. (2023) who used a preliminary CEERS MIRI dataset on a UV-selected sample of SFGs. Although this finding is also in qualitative agreement with recent ALMA studies that found compact rest-submm sizes relative to the rest-optical size–mass relation (e.g., Lang et al. 2019; Puglisi et al. 2019; Tadaki et al. 2020; Puglisi et al. 2021; Gómez-Guijarro et al. 2022a), our rest-MIR sizes are larger than the dust-obscured star formation sizes inferred from rest-submm (e.g., ~ 2.8 kpc vs. ~ 1.4 kpc at $\sim 10^{10.5} M_{\odot}$ and $z \sim 2$; Gómez-Guijarro et al. 2022a). We note, however, that this latter study is dominated by massive ($\sim 10^{10.8} M_{\odot}$) and high-redshift

($z \sim 2.5$) galaxies and thus comparison with the MIRI sample mostly relies on extrapolation of their rest-submm relation to lower masses and redshifts. The comparison between our results at rest-MIR and those at rest-submm with ALMA is discussed in depth in Sect. 5.1.

4.2.2. Rest-optical to rest-MIR size ratio

In order to analyze in more detail this mass-dependent relation between the rest-MIR and rest-optical sizes, we study in Fig. 11 the dependence of the rest-optical to rest-MIR size ratio as a function of some key physical properties of our galaxies, that is, their redshifts, stellar masses, rest-optical sizes, axis ratio, dust attenuation (A_V), and distances to the MS. It is important to note that we do not find a significant absolute offset between the rest-optical and rest-MIR centers of these galaxies, with a median and standard deviation astrometric offset of $0.02''$ (160 pc at $z = 1$) and $0.04''$ (320 pc at $z = 1$), respectively.

Four main conclusions can be drawn from Fig. 11. Firstly, galaxies above the MS (i.e., starbursts) have rest-MIR sizes that are, independently of their redshifts and stellar masses, a factor ~ 2 smaller than their rest-optical sizes. This is the most significant trend observed in Fig. 11. Starbursts are frequently associated with major mergers (e.g., Hung et al. 2013; Cibinel et al. 2019; Pearson et al. 2019) and indeed the *HST*-F160W Gini and M_{20} coefficients of our starbursts, measured using the python package Statmorph, are shifted, compared to our MS galaxies, toward the merger region defined by Lotz et al. (2008). Our finding that rest-MIR sizes are ~ 2 times smaller than rest-optical sizes supports thus the notion that merger-driven starbursts develop dusty, star-forming cores amidst disturbed optical morphologies; as observed, for example, in the local antennae galaxies (see also Puglisi et al. 2019). Secondly, the median rest-optical to rest-MIR size ratio of MS galaxies increases with their stellar masses, from $1.1^{+0.4}_{-0.2}$ at $\sim 10^{9.8} M_{\odot}$ to $1.6^{+1.0}_{-0.3}$ at $\sim 10^{11} M_{\odot}$. Thirdly, the distribution of rest-optical to rest-MIR size ratios of MS galaxies is not Gaussian but rather skewed towards high values ($\gtrsim 1.8$; see also the right panel of Fig. 12). This implies that there is a population of galaxies with compact star-forming components relative to their stellar components. Fourthly, the rest-optical to rest-MIR size ratio does not evolve with redshift and does not depend on the axis ratio.

Although the finding of increasingly larger rest-optical to rest-MIR size ratios could be interpreted as, for example, the signature of the formation of dense stellar cores in massive galaxies, one should be cautious before drawing such a conclusion. Indeed, these rest-optical sizes (at rest-frame 5000 \AA) could still be affected by negative radial color gradients and be different from the intrinsic half-stellar mass sizes of these galaxies (e.g., Suess et al. 2019, 2022; Miller et al. 2023; Zhang et al. 2023); this effect being probably more important in massive SFGs, which have larger dust attenuation than lower mass systems (Pannella et al. 2015; Gómez-Guijarro et al. 2023; Zhang et al. 2023). Larger color gradients at higher stellar masses would thus explain the increase of the rest-optical to rest-MIR size ratio with stellar mass and dust attenuation seen in Fig. 11. To investigate the effect of radial color gradient on stellar size measurements, Suess et al. (2022) used the CEERS *JWST* F150W and F440W images and compared the rest-optical sizes of $\sim 1,000$ SFGs at $1.0 < z < 2.5$ with their rest-NIR sizes (at rest-frame $1.5 \mu\text{m}$), the latter being considered the best possible proxy for the stellar mass distribution in these galaxies. They find a mass-dependent rest-optical to rest-NIR size ratio, suggesting that large radial

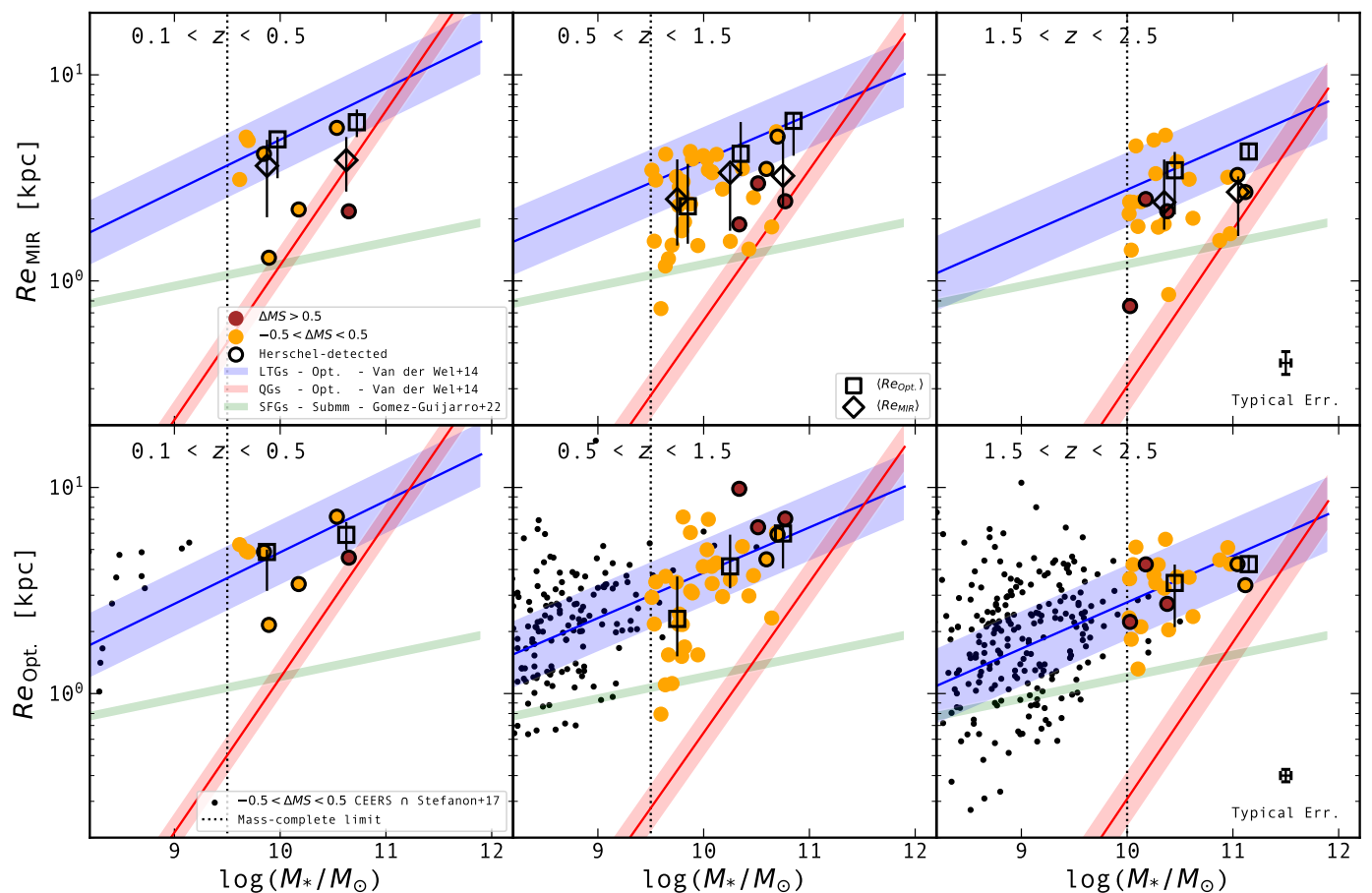


Fig. 10. Rest-MIR size–mass (*upper panels*) and rest-optical size–mass (*lower panels*) distributions of the 69 SFGs in our final sample. Circles are color-coded by the distance of each galaxy to the MS, i.e., $-0.5 < \Delta MS < 0.5$ (orange), and $\Delta MS > 0.5$ (brown). Circles outlined by black edges are detected in the FIR by *Herschel*. The rest-MIR sizes were inferred by setting $n_{\text{MIR}} = 1$ during our partial structural parameter analysis. Black dots show galaxies within the four CEERS red MIRI fields but which remained undetected in a MIRI bandpass that is dominated by dust emission (i.e., $S/N < 10$ or $S_v^{\text{dust}}/S_v^{\text{total}} < 75\%$). Open diamonds and squares show the 16th, 50th, and 84th percentiles of the rest-MIR and rest-optical size distributions in bins of stellar mass, respectively. Squares (rest-optical sizes) are reproduced in the upper panels for comparison to the rest-MIR sizes and have been shifted by 0.1 dex along the x-axis for clarity. The blue- and red-shaded regions correspond to the size–mass relation inferred in the rest-optical by [van der Wel et al. \(2014\)](#) for late-type and early-type galaxies, respectively. The green-shaded region shows the size–mass relation inferred in the submm by [Gómez-Guijarro et al. \(2022a\)](#) using mostly massive ($\sim 10^{10.8} M_\odot$) and high-redshift ($z \sim 2.5$) SFGs. Here, we assumed a mean axis ratio of 0.5 (see Fig. 7) to convert their circularized radii into semi-major axis radii. Vertical dotted lines show the mass completeness limits of our sample. Typical 1σ error bars for individual objects are shown in the upper and lower right panels.

color gradients in massive galaxies affect their rest-optical sizes, which therefore differ from their intrinsic half-stellar mass sizes. We show in the upper central panel of Fig. 11, the mass-dependent rest-optical to rest-NIR size ratio found in [Suess et al. \(2022\)](#). This relation strikingly matches that observed in our sample between our rest-optical and rest-MIR sizes. It comes that at all stellar masses, $Re_{\text{Opt.}}/Re_{\text{MIR}} \sim Re_{\text{Opt.}}/Re_{\text{NIR}}$, and thus $Re_{\text{NIR}}/Re_{\text{MIR}} \sim 1$. This implies that the mass-dependent rest-optical to rest-MIR size ratio observed in our study is likely due to radial color gradients affecting the rest-optical size measurements and that the median rest-MIR sizes are consistent, at all stellar masses, with the rest-NIR sizes and therefore with the half-stellar mass sizes of these galaxies.

Eighteen of our galaxies have a MIRI 7.7 μm band detection which is, according to our CIGALE SED fit (Sect. 2.3), dominated by their stellar component (i.e., $S_v^{\text{stellar}}/S_v^{\text{total}} > 75\%$; e.g., ID 12091; see upper panel of Fig. 1). Replacing the rest-optical sizes of these 18 galaxies by their rest-NIR sizes measured on the MIRI 7.7 μm image, significantly reduces the mass-dependent trend observed in the upper central panel of Fig. 11 (see gray

line in this panel). This reinforces the idea that our rest-optical sizes are affected by radial color gradients at high masses and that the extents of the star-forming and stellar components of the SFGs probed by our study are, on average, consistent. Future *JWST* surveys with wide overlapping NIRCcam and MIRI coverage will be essential to confirm these findings by allowing detailed measurement of the shape of the radial attenuation profiles of SFGs.

We then investigate the evolution of the rest-MIR-to-rest-optical size ratios with the distance of the rest-optical sizes from the size–mass relation of SFGs (i.e., late-type galaxies, LTGs; $Re_{\text{Opt.}}/Re_{\text{LTG}}(M_*, z)$; Fig. 12). Because we found that our rest-optical sizes and the rest-optical size–mass relation of [van der Wel et al. \(2014\)](#) were likely affected by color gradients, we corrected them using the rest-NIR-to-rest-optical size ratio versus mass relation of [Suess et al. \(2022\)](#), effectively turning these rest-optical sizes into half-mass sizes. In Fig. 12, we identify three populations of galaxies. Firstly, the largest population (C1), which contains about 61% of our galaxies and corresponds to systems with an extended stellar component (i.e., sitting within

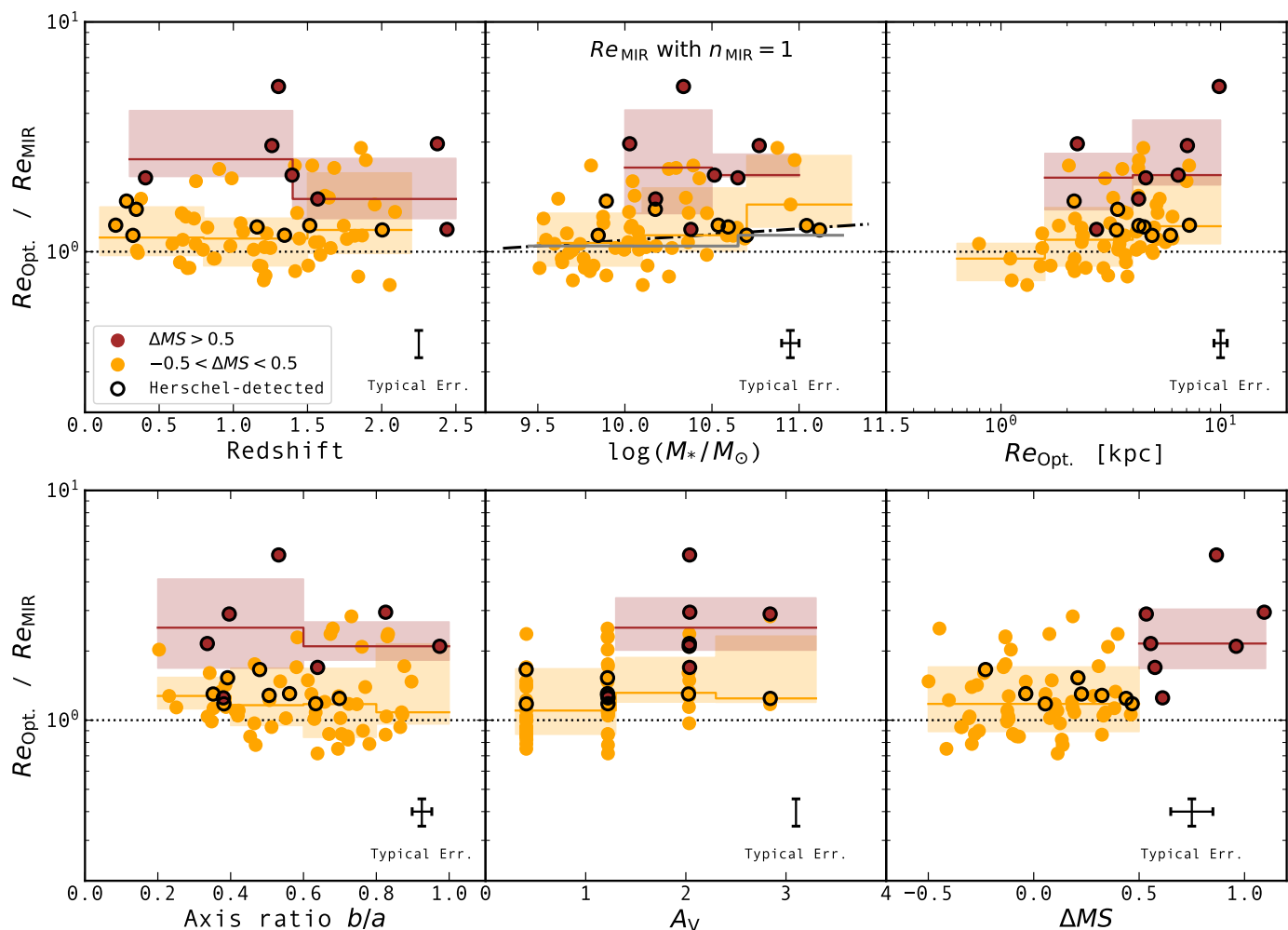


Fig. 11. Rest-optical to rest-MIR size ratios for the 69 SFGs in our final sample as a function of their redshifts, stellar masses, rest-optical sizes, axis ratio, dust attenuation, and distances to the MS. Circles are color-coded by the distance of each galaxy to the MS, i.e., $-0.5 < \Delta MS < 0.5$ (orange), and $\Delta MS > 0.5$ (brown). Circles outlined by black edges are detected in the FIR by *Herschel*. Brown line and shaded region show the median and 16th and 84th percentiles of starbursts ($\Delta MS > 0.5$) in bins of redshift, stellar mass, rest-optical effective radius, axis ratio, dust attenuation, and distance to the MS, respectively. Orange regions display the same quantities but for MS galaxies. These rest-MIR sizes were inferred by setting $n_{\text{MIR}} = 1$ during our partial structural parameter analysis. In the upper central panel, we show as dash-dotted line the mass-dependent rest-optical to rest-NIR size ratio found in [Suess et al. \(2022\)](#), and as gray line, the median for MS galaxies when replacing the rest-optical sizes of 18 galaxies by their rest-NIR sizes measured on their MIRI $7.7 \mu\text{m}$ images which are, according to our CIGALE SED fits, dominated by their stellar component. Typical 1σ error bars for individual objects are shown in each panel. The discretized values along the dust attenuation axis correspond to the sampling of this parameter used for our CIGALE fits.

or above the size–mass relation when considering their rest-optical sizes; $Re_{\text{Opt.}}^c / Re_{\text{LTG}}^c(M_*, z) > 10^{-0.19}$, i.e., within 1σ of the size–mass relation) and an equally extended star-forming component (i.e., $Re_{\text{Opt.}}^c / Re_{\text{MIR}} < 1.8$). This $Re_{\text{Opt.}}^c / Re_{\text{MIR}} \sim 1.8$ limit was set to three times the dispersion of a Gaussian function fit to the distribution of rest-optical to rest-MIR size ratios with $Re_{\text{Opt.}}^c / Re_{\text{MIR}} < 1$ (black line in Fig. 12). Secondly, a population (C3) that contains about 24% of our galaxies and corresponds to systems with a compact stellar component ($Re_{\text{Opt.}}^c / Re_{\text{LTG}}^c(M_*, z) < 10^{-0.19}$) and an equally compact star-forming component (i.e., $Re_{\text{Opt.}}^c / Re_{\text{MIR}} < 1.8$). This population of galaxies has structural properties close to those of the so-called blue nuggets, that is, galaxies which have already built their dense stellar core and could be on their way to quiescence (e.g., [Barro et al. 2017](#)). Thirdly, a population (C2) that contains about 15% of our galaxies and corresponds to systems with a compact dusty star-forming component embedded in a larger

stellar structure (i.e., $Re_{\text{Opt.}}^c / Re_{\text{MIR}} > 1.8$). Most of these galaxies also have a stellar component that lies well within the size–mass relation (i.e., $Re_{\text{Opt.}}^c / Re_{\text{LTG}}^c(M_*, z) > 10^{-0.19}$) and which can therefore be considered as extended. This new population of galaxies, which cannot be identified solely using optical images, could be the missing link between the galaxies with extended stellar component sitting on the size–mass relation and the blue nuggets with their already compact stellar component (see discussion in Sect. 5.2). We note that the fractions of galaxies in each of these three populations remain about the same if we exclude starbursts (i.e., $\Delta MS > 0.5$) or focus only on the high masses (i.e., $M_* > 10^{10.5} M_\odot$).

4.2.3. Evolution of the stellar density, Σ_1

The stellar density within the inner 1 kpc radius of a galaxy (i.e., Σ_1) is known to be a key structural parameter for SFGs

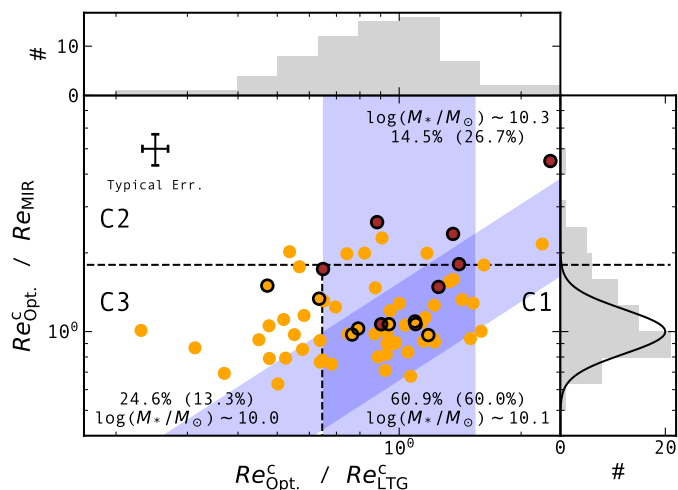


Fig. 12. Rest-optical to rest-MIR size ratios for the 69 SFGs in our final sample as a function of the distance of their rest-optical sizes to the size–mass relation of LTGs (i.e., $Re_{\text{Opt}}^c / Re_{\text{LTG}}^c(M_*, z)$). Right and upper panels present the distributions of these two quantities. Circles are color-coded by the distance of each galaxy to the MS, i.e., $-0.5 < \Delta MS < 0.5$ (orange), and $\Delta MS > 0.5$ (brown). Circles outlined by black edges are detected in the FIR by *Herschel*. A typical 1σ error bar for individual objects is shown in the upper left. Galaxies within the vertical (diagonal) blue-shaded region have their rest-optical (rest-MIR) sizes well within the size–mass relation of LTGs ($\sigma \sim 0.19$ dex; van der Wel et al. 2014). The numbers in each frame provide the median stellar mass as well as the fraction of galaxies in each of these three populations above our mass completeness limits and above $> 10^{10.5} M_{\odot}$ in parenthesis: galaxies with extended star-forming and stellar components (C1); galaxies with a compact star-forming component embedded in an extended stellar component (C2); and finally, galaxies with compact star-forming and stellar components (C3).

and QGs (e.g., Barro et al. 2017; Mosleh et al. 2017; Gómez-Guijarro et al. 2019; Suess et al. 2021). For example, QGs have significantly higher core densities than SFGs ($\Sigma_1^Q(M_*, z) > \Sigma_1^{\text{SFG}}(M_*, z)$), which suggests that on their way to quiescence SFGs must experience a phase of significant core growth relative to the average evolution of their Σ_1 along the Σ_1^{SFG} –mass relation (e.g., Barro et al. 2017). This is illustrated by the fact that the distribution of all galaxies in the EGS relative to the MS and to the Σ_1^Q –mass relation follows an L-shape (see blue contours of Fig. 13), that is, SFGs within the MS but already exhibiting a dense stellar core (i.e., blue nuggets; $\Sigma_1 \sim \Sigma_1^Q(M_*, z)$ and thus $\Delta\Sigma_1^Q \sim 0$) could be the precursors of QGs emerging at later times. We note that here Σ_1 has been calculated using the rest-optical effective radius and Sérsic index of these galaxies. We also show in Fig. 13 the distribution of our galaxies in the $\Delta MS - \Delta\Sigma_1$ plane (using as proxies of their Σ_1 their rest-optical effective radius and Sérsic index, correcting the former for color gradients using the rest-NIR-to-rest-optical size ratio versus mass relation of Suess et al. 2022). As expected, our galaxies are distributed over a broad range of $\Delta\Sigma_1$: from SFGs with relatively extended stellar component and thus light core densities to blue nuggets with their compact stellar component and thus dense core densities⁵. Using the size of the star-forming component of these galaxies, we can now go one step further than previous studies and predict the evolution along the $\Delta\Sigma_1$ axis that the on-going star formation will produce. To do so, we first assumed that the molecular

⁵ Blue nuggets are formally defined in Barro et al. (2017) as SFGs within $2\text{-}\sigma$ of the Σ_1^Q –mass relation.

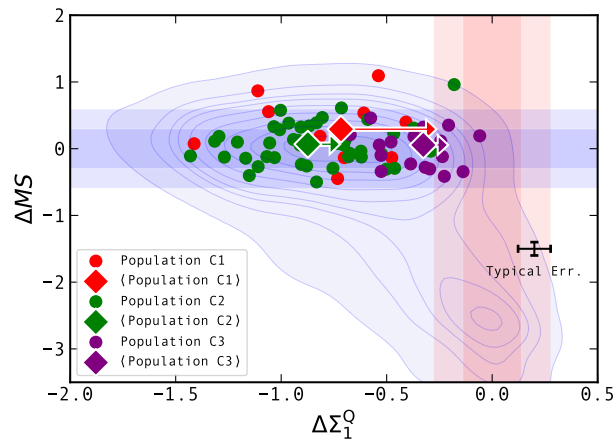


Fig. 13. Distance to the MS as a function of the distance to the mass– Σ_1 relation of QGs ($\Delta\Sigma_1^Q \equiv \log(\Sigma_1^Q(M_*, z)/\Sigma_1)$; see Barro et al. 2017) for the 69 SFGs in our final sample. Green circles correspond to the population of galaxies with extended star-forming and stellar components (C1); red circles correspond to the population of galaxies with a compact star-forming component embedded in an extended stellar component (C2); and finally, purple circles correspond to the population of galaxies with compact star-forming and stellar components (C3). Green, red, and purple diamonds show the median values of these populations. The median increases of $\Delta\Sigma_1^Q$ for these three different populations of galaxies are displayed by right-pointing arrows (see text for details of this calculation). Contours correspond to the distribution of all sources in the EGS, plotted using a kernel density estimator. The blue regions show the 1- and $2\text{-}\sigma$ dispersion of the MS, while the red regions show the 1- and $2\text{-}\sigma$ dispersion of the mass– Σ_1^Q relation. A typical 1σ error bar for individual objects is shown in the bottom right.

gas reservoir of each of our galaxies is given by the scaling relation ($M_{\text{gas}} = f(M_*, z, \Delta MS)$) of Wang et al. (2022), extrapolated, when needed, to lower stellar masses ($< 10^{10} M_{\odot}$) than those probed by their study. Then, we simply measured the increase in Σ_1 assuming that all this molecular gas is turned into stars within 600 Myrs (i.e., the typical molecular gas depletion time of these galaxies; Wang et al. 2022) and that the newly formed stars is distributed following a Sérsic index of one and according to the rest-MIR sizes of these galaxies. In doing so, we find that galaxies with an already compact stellar component and equally compact star-forming component (C3) will continue to move closer to the Σ_1^Q –mass relation, well into the blue nuggets region (i.e., within $2\text{-}\sigma$ of the Σ_1^Q –mass relation) and are thus likely the precursors of QGs. In addition, we find that while the population of galaxies with extended stellar and star-forming components (C1) will also move toward the Σ_1^Q –mass relation, their core densities will not approach those observed in blue nuggets. On the contrary, we find that galaxies with an extended stellar component but a compact star-forming component (C2) will have, within the next 600 Myrs, core densities consistent with those observed in blue nuggets. This significant increase in stellar density is naturally mostly due to the fact that star formation in this population C2 is currently taking place in compact star-forming regions.

5. Discussion

We studied the stellar (i.e., rest-optical) and dust-obscured star formation (i.e., rest-MIR) morphologies (i.e., sizes and Sérsic indices) of SFGs at $0.1 < z < 2.5$. We find that (i) the rest-MIR

Sérsic index of bright galaxies ($S/N > 75$) has a median value of $0.7^{+0.8}_{-0.3}$, which, together with their rest-MIR axis ratio distribution, suggests a disk-like morphology; (ii) the median rest-optical to rest-MIR size ratio of MS galaxies increases with their stellar mass, from $1.1^{+0.4}_{-0.2}$ at $\sim 10^{9.8} M_{\odot}$ to $1.6^{+1.0}_{-0.3}$ at $\sim 10^{11} M_{\odot}$; (iii) there exists a minor population of SFGs ($\sim 15\%$) with a compact star-forming component embedded in an extended stellar structure (i.e., $Re_{\text{Opt}}^c > 1.8 \times Re_{\text{MIR}}$). Because the unobscured SFRs of our galaxies (i.e., SFR_{UV}) are subdominant compared to their dust-obscured SFRs ($\text{SFR}_{\text{IR}}/(\text{SFR}_{\text{UV}} + \text{SFR}_{\text{IR}}) \gtrsim 0.7$ according to our CIGALE fits; see also Whitaker et al. 2017; Shen et al. 2023), in what follows, we consider the star-forming component of our galaxies as accurately traced by their dust-obscured star-forming component.

5.1. A population of compact SFGs

Our analysis reveals that about 15% (10 galaxies) of our mass-complete sample (10% if we consider only MS galaxies; 6 galaxies) have a compact star-forming component embedded in a more extended stellar structure⁶ (i.e., with $Re_{\text{Opt}}^c/Re_{\text{MIR}} > 1.8$). While this finding is consistent with those obtained in the (sub)mm with ALMA (e.g., Simpson et al. 2015; Ikarashi et al. 2015; Hodge et al. 2016; Fujimoto et al. 2017; Gómez-Guijarro et al. 2018; Elbaz et al. 2018; Lang et al. 2019; Rujopakarn et al. 2019; Puglisi et al. 2019; Franco et al. 2020; Chang et al. 2020; Chen et al. 2020; Tadaki et al. 2020; Gómez-Guijarro et al. 2022a; Zavala et al. 2022), the fraction of SFGs with such compact star-forming component appears to be very different if one considers their rest-MIR or rest-submm emissions.

To date the largest ALMA studies on the dust continuum sizes of SFGs are those of Tadaki et al. (2020) and Gómez-Guijarro et al. (2022a). Tadaki et al. (2020) studied a mass-selected sample of 85 massive ($> 10^{11} M_{\odot}$) SFGs at $z = 1.9 - 2.6$, while Gómez-Guijarro et al. (2022a) focused on a flux-limited sample of 88 massive ($M_{*}^{\text{med}} \sim 10^{10.8} M_{\odot}$) SFGs at $z = 1.5 - 4$. Both studies find that almost all SFGs have smaller dust emission regions relative to the stellar structure, with a median optical-to-(sub)mm size ratio of 2–3. This implies that more than 50% of their SFGs would satisfy our definition of a compact star-forming component embedded in an extended stellar structure. Such population, three times more numerous than ours (i.e., 50% vs 15%), suggests that compact SFGs dominate at the higher masses and redshifts probed by the Tadaki et al. (2020) and Gómez-Guijarro et al. (2022a) samples, and/or that the rest-MIR or the rest-submm emissions do not accurately trace the intrinsic sizes of the star-forming component of SFGs.

A fairer comparison in terms of redshift and stellar mass, is obtained by looking at the results of Puglisi et al. (2021). In this study, they measured the effective radius of the CO line emission of a *Herschel*-selected sample of 77 SFGs at $z = 1.1 - 1.7$ and with $M_{*} = 10^{10} - 10^{11.5} M_{\odot}$. They find that at least 46% of their SFGs exhibit a compact star-forming component embedded in an extended stellar structure. Nevertheless, their definition of compact SFGs differs from ours as it is solely based on the distance of their rest-submm sizes from the size–mass relation of LTGs, that is, $Re_{\text{submm}} < 0.5 \times Re_{\text{Opt}}^{\text{LTG}}(M_{*}, z)$. A non-negligible fraction of their compact SFGs have, however, rest-NIR sizes that are also below the size–mass relation of LTGs. Applying to their sample our more restrictive $Re_{\text{Opt}}^c/Re_{\text{MIR}} > 1.8$ criterion

⁶ This fraction would be at most 25% (20 galaxies) if we consider that all AGNs above our stellar mass complete limits and excluded from our analysis belong to this population.

would lower their fraction of compact SFGs (see Fig. 3 of Puglisi et al. 2019), rendering their and our results in better agreement. In addition, because their sample is *Herschel*-selected, it is only probing the MS at $> 10^{10.5} M_{\odot}$ and it is biased toward starbursts at $< 10^{10.5} M_{\odot}$. If the fraction of compact SFGs increases with stellar mass and distance to the MS (this latter assumption is supported by our results), this could explain the remaining disagreement between our rest-MIR and their rest-submm results.

To investigate in more detail the compatibility between our rest-MIR results and those obtained in the rest-submm with ALMA, rest-submm size measurements of a mass-selected sample of intermediate-mass MS galaxies at $z = 1 - 3$ are needed. Such constraints are, however, difficult to obtain as the detection at high angular resolution of the dust emission of intermediate-mass MS galaxies is observationally very expensive even with ALMA. To alleviate this problem, Wang et al. (2022) measured through stacking the mean rest-submm sizes of a mass-complete sample of MS galaxies at $z = 0.5 - 3$ and with $M_{*} > 10^{10} M_{\odot}$. With this statistical approach, they find that the mean rest-submm size of MS galaxies does not evolve significantly with redshift nor stellar mass, with a mean circularized half-light radius of 2.2 kpc. Assuming a mean axis ratio of 0.5 (see Fig. 7), this translates into a mean effective semi-major axis radius of 3.1 kpc, in line with our rest-MIR results (with a median value of ~ 3 kpc at $z > 0.5$ and $M_{*} > 10^{10} M_{\odot}$; see Fig. 10). While this agreement does not tell us anything about the fraction of compact SFGs as a function of stellar mass and redshift, it suggests that on average rest-MIR and rest-submm emission are probing roughly the same star-forming size. Naturally, we cannot rule out that on the galaxy-to-galaxy basis, large radial dust temperature gradients affecting the rest-submm-to-SFR relation (Popping et al. 2022) or large radial metallicity and radiation hardness gradients affecting the MIR-to-SFR relation (Schreiber et al. 2018), would yield different rest-MIR and rest-submm size measurements.

Although some discrepancies remain, our results in the rest-MIR and those in the rest-submm, unambiguously reveal that a non-negligible fraction (15%) of MS galaxies have compact star-forming component embedded in a more extended stellar structure. The origin of these compact SFGs is still highly debated. Based on the gas content and starburst-like excitation properties (Puglisi et al. 2021) of these galaxies, Gómez-Guijarro et al. (2022b) propose two scenarios to explain their formation. A first scenario in which a gas-rich merger funnels gas to the center of collision and enhances star formation in a compact star-forming region. As a result, the galaxy moves well above the MS. After few hundreds Myrs, as the gas reservoir is consumed, the SFR declines and the galaxy crosses, incidentally, the MS still exhibiting its compact star-forming component. A second scenario in which angular momentum loss, driven externally (mergers or counter-rotating streams) or internally (clump migration), funnels gas to the center of the galaxy, enhances star formation in a moderately compact star-forming region, although not well above the MS; as the gas reservoir is consumed the star-forming region becomes more compact (outside-in gas consumption) and more star formation efficient, sustaining thereby the galaxies on the MS for a relatively long time. In the case of the first scenario, the fraction of compact SFGs at a given stellar mass is thus given by the product of the mass function of SFGs and the fraction of starbursts at a given stellar mass. Because the fraction of starbursts is roughly constant (5%; Schreiber et al. 2015) and the stellar mass function of SFGs has a very steep shape (e.g., Weaver et al. 2022), one would expect that in the case of the first scenario the fraction of compact SFGs in the MS should remain constant or even decrease with mass. In contrast, in the second scenario the

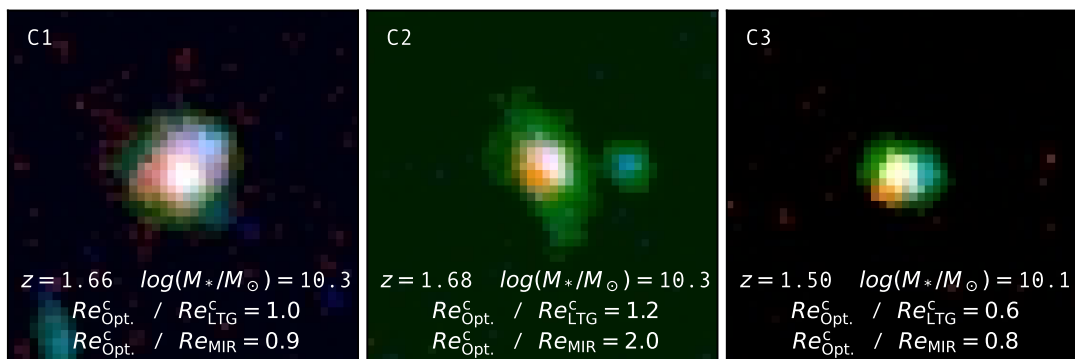


Fig. 14. Composite images (R: *JWST* F1500W – G: *HST* F160W – B: *HST* F606W) of a representative of the C1 (galaxies with extended star-forming and stellar components), C2 (galaxies with a compact star-forming component embedded in an extended stellar component), and C3 (galaxies with compact star-forming and stellar components) populations defined in Fig. 12. Each image has a size of $5'' \times 5''$.

fraction of compact SFGs in the MS is supposed to increase with mass. A significant increase with mass of the fraction of compact SFGs is suggested by the comparison of our results with those of [Tadaki et al. \(2020\)](#) and [Gómez-Guijarro et al. \(2022b\)](#), which favors the second scenario.

5.2. From extended SFGs to compact SFGs to blue nuggets, a possible evolutionary sequence

The rest-MIR sizes of MS galaxies appear to be on average smaller than those at rest-optical wavelengths and this trend increases with the stellar mass; $Re_{\text{opt}}^c / Re_{\text{MIR}}^c \sim 1.1_{-0.2}^{+0.4}$ at $\sim 10^{9.8} M_\odot$ to $1.6_{-0.3}^{+1.0}$ at $\sim 10^{11} M_\odot$. This could be interpreted as a sign that the cold gas accreted by MS galaxies is efficiently channelled into their central region and triggers the formation of their bulges (e.g., [Tonini et al. 2016](#)). Instead, we argue that this mass-dependent trend is mostly due to un-corrected negative radial color gradients, which increases their apparent rest-optical sizes; an effect that increases with stellar masses. The existence of discrepant half-light and half-mass radii in the rest-optical is supported both by observations ([Suess et al. 2019](#); [Lang et al. 2019](#); [Suess et al. 2022](#)), simulations ([Popping et al. 2022](#); [Costantin et al. 2023](#)), and radiative transfer modeling of galaxies' observed dust and structural properties ([Zhang et al. 2023](#)). Correcting statistically for this effect using the mass-dependent relation of [Suess et al. \(2022\)](#), reveals that in most SFGs (85%), the star-forming and stellar components have the same size (see Fig. 12). This population of galaxies with similar stellar and star-forming sizes must be, however, separated further into two different populations: a population of galaxies (61%) sitting on the size–mass relation of LTGs and which have thus extended stellar and star-forming components; and a smaller population of galaxies (24%) falling below the size–mass relation of LTGs and which have thus compact stellar and star-forming components (i.e., with structural properties close to those of the so-called blue nuggets). Finally, a third population, representing the remaining 15% of the SFG population, has a compact star-forming component embedded in a more extended stellar structure (i.e., with $Re_{\text{opt}}^c / Re_{\text{MIR}}^c > 1.8$). As an example, composite images of a representative of each of these populations (selected to have similar redshift and stellar mass) are shown in Fig. 14 (R: *JWST* F1500W – G: *HST* F160W – B: *HST* F606W).

Qualitatively, these three populations of galaxies, namely, the main population of extended SFGs (C1), the compact SFGs discussed in Sect. 5.1 (C2), and the population of galaxies with compact stellar component (C3), might describe an evolutionary sequence (C1→C2→C3) that follows the main phases of structural evolution in the $\Delta MS - \Delta \Sigma_1$ plane (see [Barro et al. 2017](#)): a nearly horizontal branch of MS disks growing inside-out (C1) that will transition into the compaction knee of the $\Delta MS - \Delta \Sigma_1$ plane (C3, i.e., ~blue nuggets) as a result of a significant increase in central density (C2), and lastly these blue nuggets will quench after reaching a maximum central density. In other words, the newly discovered population of MS galaxies with a compact star-forming component embedded in a more extended stellar structure would be the missing link between the main population of SFGs sitting on the size–mass and Σ_1^{SFG} –mass relations and blue nuggets with their compact stellar component and which are on their way to quiescence.

Several observational evidences support this evolutionary sequence, although care must be taken when using galaxies in a limited redshift range to sketch an evolutionary pattern. First, our main population of galaxies with extended stellar and star-forming components is qualitatively consistent with an inside-out growth scenario for disk formation (e.g., [Nelson et al. 2016](#); [Matharu et al. 2022](#)). Indeed, at least half of this population experiences ongoing star formation activity at preferentially larger radii than existing stars, and this fraction would further increase when taking into account their dust-unobscured star formation component, which is slightly larger on average than their stellar and dust-obscured star-forming components ([Shen et al. 2023](#)). The inside-out growth of this galaxy population is also suggested by the fact that their star-forming components have shallower profiles than their stellar component (i.e., $n_{\text{MIR}} < n_{\text{opt}}$), and thus that ongoing star formation would actually increase the size of their stellar component. Then, as expected in this evolutionary sequence, the distributions of extended and compact SFGs in the $\Delta MS - \Delta \Sigma_1$ plane are very similar (see green and red data points in Fig. 13). Finally, ongoing star formation in compact SFGs will increase their central densities to those observed in blue nuggets (see red arrow in Fig. 13).

Although compact SFGs seem to be the missing link between the extended SFG population and blue nuggets, the mechanism triggering a compact star-forming component embedded in a more extended stellar structure remains unknown (see Sect. 5.1).

This phase may be associated with the compaction of SFGs predicted in hydrodynamical simulations (Ceverino et al. 2015; Zolotov et al. 2015; Tacchella et al. 2016; Lapiner et al. 2023), and which is typically associated with very dissipative processes (i.e., gas-rich) like major and minor mergers (see, e.g., Fig. 14), interaction-driven gravitational instabilities, and/or strong disk instabilities (Dekel et al. 2009; Ceverino et al. 2010; Dekel & Burkert 2014; Lapiner et al. 2023). Future high-resolution observations of the stellar component (*JWST*-NIRCam and -NIRSpec) and gas reservoir (ALMA and NOEMA) of these compact SFGs will put strong observational constraints on the compaction mechanism, which is expected to take place before quenching (e.g., Barro et al. 2017).

6. Summary

We combined *HST* images from CANDELS with *JWST* images from CEERS to measure the stellar and dust-obscured star formation distributions of 69 SFGs. The rest-optical structural parameters were inferred from the *HST* F125W and F160W images, while those at rest-MIR were measured on the sharpest MIRI images (i.e., shortest wavelength) dominated by dust emission ($S_{\nu}^{\text{dust}}/S_{\nu}^{\text{total}} > 75\%$), as inferred for each galaxy from our optical-to-FIR SED fits with CIGALE. We restricted our rest-MIR full structural parameter analysis (i.e., size, Sérsic index, and ellipticity) to our brightest MIRI sample (i.e., $S/N > 75$; 35 galaxies), while we extended our study to fainter sources (i.e., $S/N > 10$; 69 galaxies) by performing a partial structural parameter analysis (i.e., size and ellipticity) by setting their Sérsic index to unity. The extension to fainter galaxies allowed us to measure and compare the rest-MIR and rest-optical sizes of a mass complete sample ($> 80\%$) of SFGs down to $10^{9.5}$, $10^{9.5}$, and $10^{10} M_{\odot}$ at $z \sim 0.3$, 1.0, and 2.0, respectively. Because the unobscured SFRs of these galaxies (i.e., SFR_{UV}) are subdominant compared to their dust-obscured SFRs (with $\text{SFR}_{\text{IR}}/(\text{SFR}_{\text{UV}} + \text{SFR}_{\text{IR}}) \gtrsim 0.7$ according to our CIGALE SED fits), one can consider that the star-forming component of our galaxies is accurately traced by their dust-obscured star-forming component. With this unique dataset, we find the following:

1. Bright galaxies ($S/N > 75$) have rest-MIR Sérsic indices with a median value of $n_{\text{MIR}} = 0.7^{+0.8}_{-0.3}$ (the range corresponds to the 16th and 84th percentiles) and the distribution of their rest-MIR axis ratio follows that of local spirals. The star-forming component of SFGs thus has a disk-like morphology.
2. The light profiles in the rest-MIR are, on average, slightly shallower than those in the rest-optical, whose median Sérsic index is $n_{\text{Opt.}} = 0.9^{+1.2}_{-0.4}$ (although a two-sample KS analysis cannot rule out the possibility that these rest-optical and rest-MIR Sérsic index distributions are drawn from the same distribution). There is only a mild correlation between n_{MIR} and $n_{\text{Opt.}}$. Hence, while the stellar and star-forming components of SFGs both have a disk-like morphology, their exact spatial distributions are intrinsically slightly different.
3. Galaxies above the MS (i.e., starbursts) have rest-MIR sizes that are, on average, a factor ~ 2 smaller than their rest-optical sizes. Because starbursts are likely triggered by major mergers, these rest-optical sizes are probably dominated by the disrupted morphology of the merging stellar components, while the rest-MIR sizes are presumably dominated by the coalescing star-forming core.
4. The median rest-optical to rest-MIR size ratio of MS galaxies increases with their stellar masses, from $1.1^{+0.4}_{-0.2}$ at $\sim 10^{9.8} M_{\odot}$

to $1.6^{+1.0}_{-0.3}$ at $\sim 10^{11} M_{\odot}$. This mass-dependent trend resembles that found in Suess et al. (2022) between the rest-optical and rest-NIR sizes of SFGs, which suggests that it is mostly due to radial color gradients affecting the rest-optical sizes. There is no significant offset between the rest-optical and rest-MIR centers of these galaxies, with a absolute median and standard deviation astrometric offset of $0.02''$ and $0.04''$, respectively.

5. Correcting statistically for the effect of radial color gradients using the mass-dependent relation of Suess et al. (2022), reveals that the median rest-optical to rest-MIR size ratio of our SFGs is $1.0^{+0.6}_{-0.2}$. In most SFGs (85%), the star-forming and stellar components thus have the same size. Of these galaxies, most fall within the size–mass relation of LTGs (61% of our total SFG sample) and thus have extended stellar and star-forming components; while a smaller fraction (24% of our total SFG sample) falls below the size–mass relation of LTGs and thus have compact stellar and star-forming components, that is, structural properties close to those of the so-called blue nuggets.
6. There exists a minor population of SFGs ($\sim 15\%$) with a compact star-forming component embedded in a more extended stellar component (i.e., $Re_{\text{Opt.}}^e > 1.8 \times Re_{\text{MIR}}$). The ongoing star formation in these compact SFGs will be sufficient to increase their central densities (i.e., Σ_1 ; bulge formation) to those observed in blue nuggets.

The three populations of galaxies revealed by our study could describe an evolutionary sequence: from disk-like SFGs growing inside-out (i.e., the extended SFG phase) that will transition into the compaction knee of the $\Delta MS - \Delta \Sigma_1$ plane (i.e., the blue nugget phase) as a result of a significant increase in their central density (i.e., the compact SFG phase). The compact SFGs would thus be the missing link between the main population of extended SFGs and the blue nuggets, the latter being on the way to quiescence. The mechanism responsible for triggering such compact star-forming components remains unknown but is expected to be associated with highly dissipative (i.e., gas-rich) processes such as major and minor mergers, interaction-driven gravitational instabilities, and/or strong disk instabilities (Dekel et al. 2009; Ceverino et al. 2010; Dekel & Burkert 2014). Future high-resolution observations of the stellar (*JWST*-NIRSpec) and gas reservoir (ALMA and NOEMA) dynamics of compact SFGs will provide strong observational constraints on the mechanisms responsible for the formation of such a compact star-forming component embedded in a larger stellar structure.

Acknowledgements. We would like to thank the referee for their comments that have helped to improve our paper. This work is based on observations made with the NASA/ESA/CSA James Webb Space Telescope. These observations are associated with program #1345. PGP-G acknowledges support from Spanish Ministerio de Ciencia e Innovación MCIN/AEI/10.13039/501100011033 through grant PGC2018-093499-B-I00. This work was supported by UNAM-PAPIIT IA102023. BM, DE, and CGG acknowledges support from CNES. BM acknowledges the following open source software used in the analysis: Astropy (Astropy Collaboration et al. 2022), photutils (Bradley et al. 2022), NumPy (Harris et al. 2020), and Statmorph (Rodríguez-Gomez et al. 2019).

References

- Arétxaga, I. 2015, in IAU General Assembly, Vol. 29, 2258051
 Astropy Collaboration, Price-Whelan, A. M., Lim, P. L., et al. 2022, *ApJ*, 935, 167
 Barro, G., Faber, S. M., Koo, D. C., et al. 2017, *ApJ*, 840, 47
 Barro, G., Pérez-González, P. G., Cava, A., et al. 2019, *ApJS*, 243, 22
 Boquien, M., Burgarella, D., Roehly, Y., et al. 2019, *A&A*, 622, A103
 Bouché, N., Dekel, A., Genzel, R., et al. 2010, *ApJ*, 718, 1001

- Bradley, L., Sipőcz, B., Robitaille, T., et al. 2022, *astropy/photutils*: 1.5.0, Zenodo
- Bruzual, G. & Charlot, S. 2003, *MNRAS*, 344, 1000
- Bushouse, H., Eisenhamer, J., Dencheva, N., et al. 2022, JWST Calibration Pipeline, Zenodo
- Calzetti, D. 2001, *PASP*, 113, 1449
- Ceverino, D., Dekel, A., & Bournaud, F. 2010, *MNRAS*, 404, 2151
- Ceverino, D., Dekel, A., Tweed, D., & Primack, J. 2015, *MNRAS*, 447, 3291
- Chabrier, G. 2003, *PASP*, 115, 763
- Chang, Y.-Y., Le Floch, E., Juneau, S., et al. 2020, *ApJ*, 888, 44
- Chen, C.-C., Harrison, C. M., Smail, I., et al. 2020, *A&A*, 635, A119
- Cheung, E., Faber, S. M., Koo, D. C., et al. 2012, *ApJ*, 760, 131
- Cibinel, A., Daddi, E., Sargent, M. T., et al. 2019, *MNRAS*, 485, 5631
- Costantin, L., Pérez-González, P. G., Vega-Ferrero, J., et al. 2023, *ApJ*, 946, 71
- Davé, R., Finlator, K., & Oppenheimer, B. D. 2012, *MNRAS*, 421, 98
- Dekel, A., Birnboim, Y., Engel, G., et al. 2009, *Nature*, 457, 451
- Dekel, A. & Burkert, A. 2014, *MNRAS*, 438, 1870
- Donley, J. L., Koekemoer, A. M., Brusa, M., et al. 2012, *ApJ*, 748, 142
- Draine, B. T., Aniano, G., Krause, O., et al. 2014, *ApJ*, 780, 172
- Elbaz, D., Daddi, E., Le Borgne, D., et al. 2007, *A&A*, 468, 33
- Elbaz, D., Dickinson, M., Hwang, H. S., et al. 2011, *A&A*, 533, A119
- Elbaz, D., Hwang, H. S., Magnelli, B., et al. 2010, *A&A*, 518, L29
- Elbaz, D., Leiton, R., Nagar, N., et al. 2018, *A&A*, 616, A110
- Finkelstein, S. L., Bagley, M. B., Ferguson, H. C., et al. 2023, *ApJ*, 946, L13
- Foreman-Mackey, D., Hogg, D. W., Lang, D., & Goodman, J. 2013, *PASP*, 125, 306
- Franco, M., Elbaz, D., Zhou, L., et al. 2020, *A&A*, 643, A30
- Fujimoto, S., Ouchi, M., Shibuya, T., & Nagai, H. 2017, *ApJ*, 850, 83
- Gardner, J. P., Mather, J. C., Clampin, M., et al. 2006, *Space Sci. Rev.*, 123, 485
- Geach, J. E., Dunlop, J. S., Halpern, M., et al. 2017, *MNRAS*, 465, 1789
- Gómez-Guijarro, C., Elbaz, D., Xiao, M., et al. 2022a, *A&A*, 658, A43
- Gómez-Guijarro, C., Elbaz, D., Xiao, M., et al. 2022b, *A&A*, 659, A196
- Gómez-Guijarro, C., Magdis, G. E., Valentino, F., et al. 2019, *ApJ*, 886, 88
- Gómez-Guijarro, C., Magnelli, B., Elbaz, D., et al. 2023, *A&A*, 677, A34
- Gómez-Guijarro, C., Toft, S., Karim, A., et al. 2018, *ApJ*, 856, 121
- Harris, C. R., Millman, K. J., van der Walt, S. J., et al. 2020, *Nature*, 585, 357
- Hodge, J. A., Swinbank, A. M., Simpson, J. M., et al. 2016, *ApJ*, 833, 103
- Hung, C.-L., Sanders, D. B., Casey, C. M., et al. 2013, *ApJ*, 778, 129
- Ikarashi, S., Ivison, R. J., Caputi, K. I., et al. 2015, *ApJ*, 810, 133
- Jiménez-Andrade, E. F., Magnelli, B., Karim, A., et al. 2019, *A&A*, 625, A114
- Jin, S., Daddi, E., Liu, D., et al. 2018, *ApJ*, 864, 56
- Kennicutt, Robert C., J. 1998, *ARA&A*, 36, 189
- Koekemoer, A. M., Faber, S. M., Ferguson, H. C., et al. 2011, *ApJS*, 197, 36
- Lang, P., Schinnerer, E., Smail, I., et al. 2019, *ApJ*, 879, 54
- Lapiner, S., Dekel, A., Freundlich, J., et al. 2023, *MNRAS*, 522, 4515
- Lilly, S. J., Carollo, C. M., Pipino, A., Renzini, A., & Peng, Y. 2013, *ApJ*, 772, 119
- Liu, D., Daddi, E., Dickinson, M., et al. 2018, *ApJ*, 853, 172
- Liu, Z., Morishita, T., & Kodama, T. 2023, arXiv e-prints, arXiv:2305.10944
- Lotz, J. M., Davis, M., Faber, S. M., et al. 2008, *ApJ*, 672, 177
- Lutz, D., Poglitsch, A., Altieri, B., et al. 2011, *A&A*, 532, A90
- Magnelli, B., Elbaz, D., Chary, R. R., et al. 2011, *A&A*, 528, A35
- Matharu, J., Papovich, C., Simons, R. C., et al. 2022, *ApJ*, 937, 16
- Miller, T. B., van Dokkum, P., & Mowla, L. 2023, *ApJ*, 945, 155
- Mortlock, A., Conselice, C. J., Hartley, W. G., et al. 2015, *MNRAS*, 447, 2
- Mosleh, M., Tacchella, S., Renzini, A., et al. 2017, *ApJ*, 837, 2
- Murphy, E. J., Momjian, E., Condon, J. J., et al. 2017, *ApJ*, 839, 35
- Nelson, E. J., van Dokkum, P. G., Brammer, G., et al. 2012, *ApJ*, 747, L28
- Nelson, E. J., van Dokkum, P. G., Momcheva, I., et al. 2013, *ApJ*, 763, L16
- Nelson, E. J., van Dokkum, P. G., Momcheva, I. G., et al. 2016, *ApJ*, 817, L9
- Noeske, K. G., Faber, S. M., Weiner, B. J., et al. 2007, *ApJ*, 660, L47
- Nordon, R., Lutz, D., Genzel, R., et al. 2012, *ApJ*, 745, 182
- Oliver, S. J., Bock, J., Altieri, B., et al. 2012, *MNRAS*, 424, 1614
- Pannella, M., Elbaz, D., Daddi, E., et al. 2015, *ApJ*, 807, 141
- Pearson, W. J., Wang, L., Alpaslan, M., et al. 2019, *A&A*, 631, A51
- Peng, Y.-j. & Maiolino, R. 2014, *MNRAS*, 443, 3643
- Pérez-González, P. G., Barro, G., Annunziatella, M., et al. 2023, *ApJ*, 946, L16
- Perrin, M. D., Sivaramakrishnan, A., Lajoie, C.-P., et al. 2014, in *Society of Photo-Optical Instrumentation Engineers (SPIE) Conference Series*, Vol. 9143, *Space Telescopes and Instrumentation 2014: Optical, Infrared, and Millimeter Wave*, ed. J. Oschmann, Jacobus M., M. Clampin, G. G. Fazio, & H. A. MacEwen, 91433X
- Popping, G., Pillepich, A., Calistro Rivera, G., et al. 2022, *MNRAS*, 510, 3321
- Puglisi, A., Daddi, E., Liu, D., et al. 2019, *ApJ*, 877, L23
- Puglisi, A., Daddi, E., Valentino, F., et al. 2021, *MNRAS*, 508, 5217
- Rathaus, B. & Sternberg, A. 2016, *MNRAS*, 458, 3168
- Rodríguez, S. & Padilla, N. D. 2013, *MNRAS*, 434, 2153
- Rodríguez-Gomez, V., Snyder, G. F., Lotz, J. M., et al. 2019, *MNRAS*, 483, 4140
- Rujopakarn, W., Daddi, E., Rieke, G. H., et al. 2019, *ApJ*, 882, 107
- Schreiber, C., Elbaz, D., Pannella, M., et al. 2018, *A&A*, 609, A30
- Schreiber, C., Pannella, M., Elbaz, D., et al. 2015, *A&A*, 575, A74
- Shen, L., Papovich, C., Yang, G., et al. 2023, *ApJ*, 950, 7
- Simpson, J. M., Smail, I., Swinbank, A. M., et al. 2015, *ApJ*, 807, 128
- Stalevski, M., Ricci, C., Ueda, Y., et al. 2016, *MNRAS*, 458, 2288
- Stefanon, M., Yan, H., Mobasher, B., et al. 2017, *ApJS*, 229, 32
- Suess, K. A., Bezanson, R., Nelson, E. J., et al. 2022, *ApJ*, 937, L33
- Suess, K. A., Kriek, M., Price, S. H., & Barro, G. 2019, *ApJ*, 885, L22
- Suess, K. A., Kriek, M., Price, S. H., & Barro, G. 2021, *ApJ*, 915, 87
- Szalay, A. S., Connolly, A. J., & Szokoly, G. P. 1999, *AJ*, 117, 68
- Tacchella, S., Carollo, C. M., Förster Schreiber, N. M., et al. 2018, *ApJ*, 859, 56
- Tacchella, S., Dekel, A., Carollo, C. M., et al. 2016, *MNRAS*, 457, 2790
- Tacchella, S., Lang, P., Carollo, C. M., et al. 2015, *ApJ*, 802, 101
- Tacchella, S., Smith, A., Kannan, R., et al. 2022, *MNRAS*, 513, 2904
- Tadaki, K.-i., Belli, S., Burkert, A., et al. 2020, *ApJ*, 901, 74
- Tonini, C., Mutch, S. J., Croton, D. J., & Wyithe, J. S. B. 2016, *MNRAS*, 459, 4109
- van der Wel, A., Franx, M., van Dokkum, P. G., et al. 2014, *ApJ*, 788, 28
- van Dokkum, P. G., Leja, J., Nelson, E. J., et al. 2013, *ApJ*, 771, L35
- van Dokkum, P. G., Nelson, E. J., Franx, M., et al. 2015, *ApJ*, 813, 23
- Wang, T., Schreiber, C., Elbaz, D., et al. 2019, *Nature*, 572, 211
- Wang, T.-M., Magnelli, B., Schinnerer, E., et al. 2022, *A&A*, 660, A142
- Weaver, J. R., Davidzon, I., Toft, S., et al. 2022, arXiv e-prints, arXiv:2212.02512
- Whitaker, K. E., Pope, A., Cybulski, R., et al. 2017, *ApJ*, 850, 208
- Wilman, D. J., Fossati, M., Mendel, J. T., et al. 2020, *ApJ*, 892, 1
- Wuyts, S., Förster Schreiber, N. M., Genzel, R., et al. 2012, *ApJ*, 753, 114
- Wuyts, S., Förster Schreiber, N. M., Lutz, D., et al. 2011a, *ApJ*, 738, 106
- Wuyts, S., Förster Schreiber, N. M., van der Wel, A., et al. 2011b, *ApJ*, 742, 96
- Yang, G., Boquien, M., Buat, V., et al. 2020, *MNRAS*, 491, 740
- Yang, G., Caputi, K. I., Papovich, C., et al. 2023a, *ApJ*, 950, L5
- Yang, G., Papovich, C., Bagley, M., et al. 2023b, arXiv e-prints, arXiv:2307.14509
- Zavala, J. A., Aretxaga, I., Geach, J. E., et al. 2017, *MNRAS*, 464, 3369
- Zavala, J. A., Casey, C. M., Spilker, J., et al. 2022, *ApJ*, 933, 242
- Zhang, J., Wuyts, S., Cutler, S. E., et al. 2023, *MNRAS*, 524, 4128
- Zolotov, A., Dekel, A., Mandelker, N., et al. 2015, *MNRAS*, 450, 2327

¹ Université Paris-Saclay, Université Paris Cité, CEA, CNRS, AIM, 91191, Gif-sur-Yvette, France

² Department of Physics and Astronomy, Texas A&M University, College Station, TX, 77843-4242 USA

³ George P. and Cynthia Woods Mitchell Institute for Fundamental Physics and Astronomy, Texas A&M University, College Station, TX, 77843-4242 USA

⁴ NSF's National Optical-Infrared Astronomy Research Laboratory, 950 N. Cherry Ave., Tucson, AZ 85719, USA

⁵ Department of Astronomy, The University of Texas at Austin, Austin, TX, USA

⁶ Department of Astronomy, University of Michigan, 1085 South University Avenue, Ann Arbor, MI 48109-1107, USA

⁷ Aix Marseille Univ, CNRS, CNES, LAM Marseille, France

⁸ Centro de Astrobiología (CAB), CSIC-INTA, Ctra. de Ajalvir km 4, Torrejón de Ardoz, E-28850, Madrid, Spain

⁹ Astrophysics Science Division, NASA Goddard Space Flight Center, 8800 Greenbelt Rd, Greenbelt, MD 20771, USA

¹⁰ Instituto de Radioastronomía y Astrofísica, Universidad Nacional Autónoma de México, Antigua Carretera a Pátzcuaro #8701, Ex-Hda. San José de la Huerta, Morelia, Michoacán, México C.P. 58089

¹¹ Laboratory for Multiwavelength Astrophysics, School of Physics and Astronomy, Rochester Institute of Technology, 84 Lomb Memorial Drive, Rochester, NY 14623, USA

¹² Space Telescope Science Institute, 3700 San Martin Dr., Baltimore, MD 21218, USA

¹³ ESA/AURA Space Telescope Science Institute

¹⁴ Kavli Institute for Cosmology, University of Cambridge, Madingley Road, Cambridge, CB3 0HA, UK

¹⁵ Cavendish Laboratory, University of Cambridge, 19 JJ Thomson Avenue, Cambridge, CB3 0HE, UK

¹⁶ Department of Physics and Astronomy, University of California, 900 University Ave, Riverside, CA 92521, USA

¹⁷ Department of Physics, University of Bath, Claverton Down, Bath, BA2 7AY, UK

¹⁸ Kapteyn Astronomical Institute, University of Groningen, P.O. Box 800, 9700 AV Groningen, The Netherlands

¹⁹ SRON Netherlands Institute for Space Research, Postbus 800, 9700 AV Groningen, The Netherlands

²⁰ National Astronomical Observatory of Japan, 2-21-1 Osawa, Mitaka, Tokyo 181-8588, Japan